

1 **Modeling of aerosol property evolution during winter haze**
2 **episodes over a megacity cluster in northern China: Roles of**
3 **regional transport and heterogeneous reactions of SO₂**

4 Huiyun Du^{1,2}, Jie Li^{1,2,3*}, Xueshun Chen¹, Zifa Wang^{1,2,3}, Yele Sun^{1,2,3}, Pingqing Fu¹,
5 Jianjun Li⁴, Jian Gao⁵, Ying Wei^{1,2}

6 ¹ LAPC, Institute of Atmospheric Physics, Chinese Academy of Sciences, Beijing
7 100029, China

8 ² College of Earth Sciences, University of Chinese Academy of Sciences, Beijing
9 100029, China

10 ³ Center for Excellence in Urban Atmospheric Environment, Institute of Urban
11 Environment, Chinese Academy of Sciences, Xiamen, China

12 ⁴ China National Environmental Monitoring Center, Beijing, China

13 ⁵ Chinese Research Academy of Environmental Sciences

14 **Abstract.** Regional transport and heterogeneous reactions played crucial roles in haze
15 formation over a megacity cluster centered on Beijing. In this study, the updated Nested
16 Air Quality Prediction Model System (NAQPMS) and the HYSPLIT Lagrangian
17 trajectory model were employed to investigate the evolution of aerosols—in terms of
18 the number concentration, size distribution, and aging degree—in Beijing during six
19 haze episodes between November 15 and December 15, 2016, as part of the Air
20 Pollution and Human Health–Beijing (APHH-Beijing) winter campaign of 2016. The
21 model exhibited reasonable performance not only in mass concentrations of PM_{2.5} and
22 its components in Beijing but also in the number concentration, size distribution, and
23 aging degree. We revealed that regional transport played a nonnegligible role in haze
24 episodes, with contributions of 14%–31% to the surface PM_{2.5} mass concentration. The
25 contribution of regional transport to secondary inorganic aerosols was larger than that
26 to primary aerosols (30%–63% vs. 3%–12%). The chemical transformation of SO₂ in
27 the transport pathway from source regions to Beijing was the major source of SO₄²⁻.
28 We also found that sulfate formed outside Beijing from SO₂ emitted in Beijing; this
29 sulfate was then blown back to Beijing and considerably influenced haze formation. In
30 the transport pathway, aerosols underwent aging, which altered the mass ratio of coating

31 to black carbon (R_{BC}) and the size distribution of number concentrations. During the
32 episodes, the geometric mean diameter (GMD) increased from less than 100 nm at the
33 initial site to approximately 120 nm at the final site (Beijing), and R_{BC} increased from
34 2–4 to 4–8. In haze episodes with high humidity, the average contributions of gas and
35 aqueous chemistry, heterogeneous chemistry, and primary emission to sulfate were
36 comparable. But their relative contributions varied with pollution levels. Primary
37 emissions had the greatest impact under light to moderate pollution levels, whereas
38 heterogeneous chemistry had a stronger effect under high pollution levels.

39 **Keywords:** Regional transport; heterogeneous reactions; number size distribution;
40 NAQPMS

41 **1 Introduction**

42 In past decades, a megacity cluster in China that is centered on Beijing and
43 includes 28 cities (272,500 km², a population of 191.7 million people) has experienced
44 frequent severe and persistent haze episodes (Zhao et al., 2013; Sun et al., 2014; Sun et
45 al., 2016). PM_{2.5} levels exceeding 500 $\mu\text{g m}^{-3}$ have often been reported. The adverse
46 effects of PM_{2.5} on visibility, climate, and particularly human health have drawn
47 widespread public attention (Hyslop, 2009; Chen et al., 2018; Yang et al., 2017a; Yang
48 et al., 2017b; Anderson et al., 2010). Although the PM_{2.5} concentration in Beijing has
49 decreased by 35% in the recent 5 years (2013–2017) benefiting from implementation
50 of the Atmospheric Pollution Prevention and Control Action Plan, the PM_{2.5} level in
51 2017 still reached 58 $\mu\text{g m}^{-3}$, which is 1.7 times the World Health Organization-
52 recommended safe level of 35 $\mu\text{g m}^{-3}$
53 (<http://www.bjepb.gov.cn/bjhrb/index/index.html>). Understanding the mechanism of
54 haze episodes in this megacity cluster is thus an urgent task for policymakers.

55 Observations have revealed that haze episodes in this megacity cluster are mainly
56 caused by the rapid formation of secondary inorganic species (SIA, including sulfate,
57 nitrate, and ammonium) (Huang et al., 2014; Zheng et al., 2015; Han et al., 2016). The
58 SIA mass fraction in PM_{2.5} can be up to 55% on severe pollution days, which is 2.5

59 times that on clear days (Ma et al., 2017). Tang et al. (2016a) proposed that local
60 chemical transformation associated with humidity dominated the rapid formation of
61 SIA in Beijing. Yang et al. (2015) argued that local chemical conversion would not be
62 fully able to explain the observed rapid formation of SIA in a short time. Using a
63 ceilometer and in situ observation data, Zhu et al. (2016) and Ma et al. (2017) further
64 proposed that regional transport was the major cause of the initial haze stage and that
65 local chemistry, particularly heterogeneous chemistry, dominated the later rise in
66 Beijing. This result is different from the findings of modeling studies (Timmermans et
67 al., 2017; Li and Han, 2016; Li et al., 2017), in which regional transport was identified
68 as the dominant factor during haze episodes in the megacity cluster. Comprehensive
69 observations of the physicochemical properties (e.g., mixing state, number
70 concentration, and size distribution) of aerosols can provide more insights into the
71 accuracy of regional transport and chemistry assessment. Black carbon (BC) is usually
72 more thickly coated by SIA and organic aerosols in transported and aged air masses
73 than in fresh particles, as indicated by higher fractal dimension (Wang et al., 2017b),
74 larger coating fraction (ratio of variation in BC mass equivalent diameter to initial BC
75 diameter, $\Delta D_{me}/D_{me,0}$) (Peng et al., 2016) and the higher mass ratio of coating to BC
76 (R_{BC}) (Wang et al., 2018a). Massoli et al. (2015) and Wang et al. (2017) reported that
77 R_{BC} exceeded 10 in remote sites after BC had undergone long-term transport. This value
78 was much higher than that in an urban area with high fresh particle emissions, where
79 R_{BC} generally was less than 1.5 (Liu et al., 2017). The geometric mean diameter (GMD)
80 of $PM_{2.5}$ also changed significantly due to the impact of regional transport. In haze
81 episodes in Beijing, the GMD increased to 120 nm in regionally transported air masses,
82 which was twice that under clean conditions (Ma et al., 2017). Investigating the
83 evolution of aerosol properties other than mass concentration during regional transport
84 is thus useful for assessing the roles of regional and local chemistry. Such investigations
85 are rarely conducted using the current three-dimensional chemical transport models.
86 The current models generally account for only a part of the observed SO_4^{2-}
87 concentrations (Wang et al., 2014a). Heterogeneous chemistry is considered critical to

88 improving model performance (Zheng et al., 2015; Cheng et al., 2016; Li et al., 2018).
89 The treatment of heterogeneous chemistry is likely another source of modeling
90 uncertainty. Studies found that uptake coefficients (γ) were dynamically related to
91 aerosol liquid water and aerosol mix states (coating thickness) (Riemer et al., 2009;
92 Morgan et al., 2015). Although these parameters are obtained in some observation
93 studies (Bian et al., 2014; Zhang et al., 2016). The parameterization of heterogeneous
94 has rarely been linked to these parameters in previous studies (Morgan et al., 2015;
95 Zheng et al., 2015; Li et al., 2018).

96 From November 15 to December 15, 2016, a field campaign was carried out in
97 Beijing within the framework of the UK-China Air Pollution & Human Health (APHH)
98 project. Details can be seen in Shi et al. (2018). Aerosol properties such as the size
99 distribution, number concentration, and mixing states were simultaneously measured in
100 China. APHH-Beijing aimed to explore the sources and processes affecting urban
101 atmospheric pollution in Beijing. In this study, we used the NAQPMS to simulate
102 aerosol properties in the campaign period as a part of the APHH research. To improve
103 model performance, the NAQPMS was updated by incorporating an advanced particle
104 microphysics (APM) module that explicitly accounts for the microphysical process
105 (Chen et al., 2014) and a new heterogeneous chemistry scheme (Li et al., 2018). The
106 hybrid single-particle Lagrangian integrated trajectory model (HYSPLIT) was also
107 employed to explicate the evolution of aerosol properties (e.g., mixing state, number
108 concentration, and size distribution). Detailed analysis of the transport of precursors or
109 secondary products, and heterogeneous reactions was mainly focused on sulfate, as
110 recent studies indicated that sulfate is a key driver for severe haze events (Huang et al.,
111 2014; Zheng et al., 2015). Crucially, the effects of regional transport and heterogeneous
112 chemistry of SO₂ on aerosol properties were quantified. To our knowledge, this is the
113 first study to distinguish the contributions of transport of SIA itself and its precursors
114 to PM_{2.5} in Beijing, and combine trajectories with microphysical properties evolution.
115 We believe that this study is helpful to understanding the causes of haze in this megacity
116 cluster.

117 **2 Model description and methodology**

118 **2.1 Model description**

119 The Nested Air Quality Prediction Model System (NAQPMS) developed by the
120 Institute of Atmospheric Physics, Chinese Academy of Sciences (IAP/CAS) is a three-
121 dimensional Eulerian terrain-following chemical transport model. WRFv3.6.1, driven
122 by Final Analysis (FNL) data from the National Centers for Environmental Prediction
123 (NCEP), provides the meteorology field for the NAQPMS. The NAQPMS includes
124 emission, horizontal and vertical advection and diffusion, dry and wet deposition, and
125 chemical (including gas, aqueous, and heterogeneous) reaction processes (Wang et al.,
126 2001; Li et al., 2012; Li et al., 2018). In the model, aqueous chemistry happens only in
127 cloud water, including the oxidation reactions of S(IV) by O₃, H₂O₂, methyl
128 hydroperoxide, peroxyacetic acid and oxidation catalysis of transition metal ions (Fe³⁺
129 and Mn²⁺). Heterogeneous chemistry reactions happen on aerosol's surface with
130 aqueous layer and are related with aerosol liquid water. For sulfate, assuming that the
131 upper limit of γ_{SO_2} does not exceed the uptake coefficient on dust surfaces, the upper
132 limit of γ_{SO_2} is 10⁻⁴ for aerosol water content (AWC) > 300 $\mu\text{g m}^{-3}$ and its lower limit
133 is 10⁻⁶ if AWC < 10 $\mu\text{g m}^{-3}$. More details can be found in Li et al. (2018). It also
134 incorporates online source tagging, process analysis, an online WRF coupler, and other
135 techniques (Wu et al., 2017; Wang et al., 2014b). The Carbon Bond Mechanism version-
136 Z (CBMZ) is used for gas-phase chemistry mechanisms. The thermodynamic model
137 ISORROPIAII.7 is used to calculate the composition and phase state of an NH₄⁺-
138 SO₄²⁻-NO₃⁻-Cl⁻-Na⁺-H₂O inorganic aerosol system (Nenes et al., 1998). Six
139 secondary organic aerosols (SOA) are managed using a two-product module. Further
140 details of the NAQPMS can be found in the studies of Li et al. (2013, 2014, 2017), and
141 numerous subsequent papers have been published describing recent updates.

142 To accurately describe aerosol properties (e.g., number concentration, size
143 distribution, and mixing states), an advanced multitype, multicomponent, size-resolved
144 microphysics (APM) module is coupled to the NAQPMS (Chen et al., 2014). APM

145 explicitly describes microphysical aerosol processes, including nucleation,
146 condensation, evaporation, coagulation, thermodynamic equilibrium with local
147 humidity, hygroscopic growth, and dry and wet deposition (Yu and Luo, 2009), and it
148 has already been applied in the global GEOS-Chem model (Ma et al., 2014). In the
149 updated NAQPMS, 40 sectional bins covering 0.0012–12 μm were used to represent
150 secondary particle distribution (SO_4^{2-} , NO_3^- , NH_4^+ , and secondary organic aerosols)
151 (Chen et al., 2014). The size distribution of BC and primary organic aerosol was
152 represented using 28 section bins. Other primary particles such as dust and sea salt were
153 represented using four bins. The coating of secondary species on primary particles (sea
154 salt, BC, OC, and dust) was explicitly simulated using a scheme that dynamically
155 calculates the aerosol aging time with an hourly resolution on the basis of aerosol
156 microphysics. Mixing state is assumed to be semi-external. Primary particles coated
157 with SIA or SOA are considered as core-shell mixing while nucleated secondary
158 particle is internally mixed (Chen et al., 2014). The mass concentrations of coating
159 species were also tracked in the model. Chen et al. (2017) employed the updated
160 NAQPMS and revealed that the daytime aging time of BC in Beijing can be less than
161 2 hours in winter. This is much less than the fixed aging time scale of 1.2 days that has
162 been stipulated in previous studies (Liu et al. 2009) but is close to observed levels (2–
163 4 hours) (Peng et al. 2016). Li et al. (2018) further developed a heterogeneous chemical
164 scheme based on mixing states to reproduce the chemical transformation of gaseous
165 precursors on aerosol surface, which largely altered the sizes and hygroscopicity of
166 particles. Heterogeneous chemistry includes oxidation of S(IV) on aqueous layer of
167 aerosols and it is parameterized according to the scheme of Li et al. (2018). Comparison
168 with long-term observations has proven that the updated NAQPMS can successfully
169 estimate aerosol mass and the number concentration, size distribution, mixing states,
170 and BC aging time in China (Li et al., 2017b, 2018; Chen et al., 2014, 2017).

171 Distinguishing the contributions of the transport of SIA itself and its precursors to
172 $\text{PM}_{2.5}$ is always difficult (Sun et al., 2014; Li et al., 2014, 2017; Ying et al., 2014). These
173 contributions have generally been named regional transport in studies; this leads to

174 ambiguity in regional transport. In this study, we divided the secondary species (e.g.,
 175 SIA) in the i^{th} receptor region into four parts: 1) SIA locally produced from the i^{th} region
 176 locally emitted precursors (LC); 2) SIA chemically formed in other regions from the i^{th}
 177 region locally emitted precursors (LTC); 3) SIA chemically formed in the transport
 178 pathway to the i^{th} receptor region from precursors emitted in the j^{th} source region (RTC);
 179 and 4) SIA produced in the j^{th} region from precursors emitted in the j^{th} source region
 180 (RLC).

181 An online tracer-tagging module in the NAQPMS was used to resolve the
 182 contributions from LC, LTC, RTC, and RLC. The module is capable of tracing both the
 183 emission regions of precursors and the formation regions of secondary aerosols. First,
 184 the mass contribution from the locations in which SIA was formed, called C_2 , was
 185 tagged. The mass contribution from precursors emitted in different locations, called C_1 ,
 186 was then tagged. More technical details can be found in the studies of Li et al. (2014)
 187 and Wu et al. (2017). The following equation can be employed to calculate the degree
 188 of chemical conversion during transport (TC):

$$189 \quad \text{TC} = \sum_{i=1}^n (C_{1i} - C_{2i} \times CC_i) \quad (1)$$

190 Where i means region, n is the total number of regions, and n is 10 in this study. C_{1i}
 191 refers to the absolute mass concentration transported to the receptor site, produced by
 192 precursors emitted in region i ;

193 C_{2i} refers to the absolute mass concentration formed in region i and transported to
 194 receptor site;

195 CC_i refers to the local contribution ratio of precursors in region i ;

196 $C_{2i} \times CC_i$ refers to the absolute mass transported to receptor site and generated at
 197 region i by chemical conversion of precursors released at region i . When $i = 1$, it refers
 198 to LC; when $i \neq 1$, $\sum_{i=2}^n C_{2i} \times CC_i$ refers to RLC;

199 $C_{1i} - C_{2i} \times CC_i$ is the mass concentration generated in all regions except i by chemical
 200 conversion of the precursors released at region i and finally transported to the receptor
 201 site. When $i = 1$, it refers to LTC; when $i \neq 1$, $\sum_{i=2}^n (C_{1i} - C_{2i} \times CC_i)$ refers to RTC.

202 In this study, 10 regions according to administrative division are selected for

203 source tagging (Fig. 1c), six of which—Chengde, Zhangjiakou, and Qinhuangdao
204 (NHB); Beijing (BJ); Tianjin (LT); Hengshui, Xingtai, and Handan (SHB); Baoding
205 and Shijiazhuang (WHB); and Tangshan, Langfang, and Cangzhou (EHB)—are parts
206 of the Beijing–Tianjin–Hebei (BTH) area. Henan (HN), Shandong (SD), Shanxi (SX),
207 and other regions (OT) are regions outside the BTH area.

208 **2.2 Model configuration**

209 Simulation was conducted from November 10 to December 15, 2016, and the first
210 5 days were set aside as a spin-up period. The three nested model domains were shown
211 in Fig. 1a. The horizontal resolutions were 27, 9, and 3 km from the coarsest to
212 innermost domain. The first level of the NAQPMS was approximately 20 m in height,
213 and there were approximately 17 layers under 2 km.

214 To quantitatively assess the contribution of primary emissions, traditional
215 chemistry reactions (gas-phase and aqueous chemistry reactions), and heterogeneous
216 formation of sulfate, three sensitivity simulations were conducted. The baseline
217 scenario (Base) involving all heterogeneous reactions considered primary sulfate
218 emissions and its results were used for model verification and source apportionment
219 analysis. Control 1 (C1) involved all heterogeneous reactions but did not consider
220 primary sulfate emissions. Compared with Base, Control 2 (C2) excluded the
221 heterogeneous reactions of SO₂. Base–C2 represents the effect of heterogeneous
222 reactions on sulfate. Base–C1 represents contribution of primary sulfate emissions.

223 The HYSPLIT model was used to analyze the trajectories of air masses (Draxler
224 and Hess, 1998). The calculated trajectories are helpful to resolving the evolution of
225 aerosol properties in the transport pathway by extracting the simulated results by the
226 NAQPMS along trajectories. In this study, the same meteorology data (obtained hourly
227 data of the third domain) used in the NAQPMS were employed to perform trajectory
228 analysis; this avoided the errors caused by inconsistency between the two models (the
229 NAQPMS and HYSPLIT).

230 **2.3 Emission inventory**

231 The anthropogenic emissions were obtained from the $0.25^\circ \times 0.25^\circ$ Multi-
232 resolution Emission Inventory for China (MEIC), and the base year was 2016 for BTH
233 (<http://www.meicmodel.org/publications.html>). In addition, observation data collected
234 at sites within BTH were used to update the MEIC on the basis of their latitude and
235 longitude information. Biomass burning emissions were taken from the Fire Inventory
236 from NCAR (National Center for Atmospheric Research) (Wiedinmyer et al., 2011).
237 Primary sulfate was assumed to constitute 5% of SO₂ emissions in the original MEIC
238 inventory. Cao et al. (2014), Wang et al. (2009), Zheng et al. (2013), and Ma et al. (2015)
239 discovered that primary sulfate comprised large amounts of primary PM_{2.5} from
240 industrial, power, and residential emissions in the main form of (NH₄)₂SO₄ through in
241 situ measurement of source profiles. Thus, we took 40%, 6% and 15% of primary PM_{2.5}
242 from industrial, power and residential emissions, respectively, as primary sulfate
243 emissions in the inventory. Figure 1b displays the hourly primary PM_{2.5} emission rate.

244 **2.4 Observations**

245 The surface meteorological parameters were obtained from the China
246 Meteorological Administration, whereas the vertical profiles of meteorological
247 parameters were obtained from the University of Wyoming
248 (<http://weather.uwyo.edu/upperair/sounding.html>). Observations of PM_{2.5}, SO₂, NO₂,
249 and O₃ concentrations were obtained from the China National Environmental
250 Monitoring Center (<http://www.cnemc.cn/>). Aerosol components (including organic
251 matters [OM], sulfate, nitrate, and ammonium) were measured in situ at Beijing using
252 an Aerodyne high-resolution time-of-flight aerosol mass spectrometer. Details of the
253 instruments can be found in the study by Sun et al. (2015). A seven-wavelength
254 Aethalometer (AE33, Magee Scientific Corp.) was used to measure BC at Beijing (Xie
255 et al., 2018). The OC/EC in aerosol was measured by a field semi-online OC/EC
256 analyzer from Sunset Laboratory Inc. (USA) with a PM_{2.5} cyclone inlet at Tianjin and

257 Lang Fang (Gao et al., 2016). Two same ambient ion monitors (AIM; Model URG
258 9000D, URG Corporation) were used to measure hourly concentrations of water-
259 soluble ions in PM_{2.5}, including NH₄⁺, Na⁺, K⁺, Ca²⁺, Mg²⁺, SO₄²⁻, NO₃⁻ and Cl⁻ at TJ
260 and LF (Gao et al., 2016). The particle number size distributions at ground level were
261 obtained using a scanning mobility particle sizer (SMPS) with a time resolution of 5
262 min. Details of the instruments can be found in the study by Du et al. (2017). All data
263 in this study are presented in Beijing local time (UTC + 8 h).

264 **3 Model validation**

265 **3.1 PM_{2.5} mass and number concentrations and aging degrees**

266 The time series of simulated and observed PM_{2.5} in different cities of BTH from
267 November 15 to December 15, 2016, are illustrated in Fig. 2. During the study period,
268 six regional haze episodes were identified, namely, November 15–20 (Ep1), November
269 23–26 (Ep2), November 28–30 (Ep3), December 2–4 (Ep4), December 6–8 (Ep5),
270 December 10–12 (Ep6). The PM_{2.5} mass concentration frequently exceeded 200 µg m⁻³
271 and the average concentration reached 120 µg m⁻³ during episodes. Haze usually
272 formed in several hours; for example, the increasing rate of PM_{2.5} reached 200 µg m⁻³
273 h⁻¹ and lasted approximately 12 hours in Tangshan. These observed haze patterns were
274 generally reproduced by the NAQPMS. The correlation coefficient (R) between the
275 observation and simulation in most cities was 0.6–0.8, and 60%–80% of simulation
276 results were within a factor of 2 of the observation. The mean fractional bias (MFB)
277 and mean fractional error (MFE) ranged from -0.07 to 0.7, meeting the criteria of MFB
278 ≤ 0.6 and MFE ≤ 0.75 (Boylan et al., 2006). The simulation did however underestimate
279 PM_{2.5} in Beijing and Baoding for Ep2. This was caused by the failure of the mineral
280 aerosol transport simulation. Compared with other cities in the cluster, Beijing and
281 Baoding are closer to the Gobi Desert, a major dust source in East Asia, and they are
282 thus more easily affected by dust storm transport. Pan et al. (2018) found a pronounced
283 peak in the size distribution at 4–5 µm for Ep2 in Beijing. The concentrations of Ca²⁺

284 was 7 times the campaign averages (Fig. S1).

285 The aerosol components in Beijing, Langfang, and Baoding are compared in Fig.
286 3. In general, the simulation largely reproduced the variation in primary and secondary
287 aerosols. In particular, the rapid increase in SIA during Ep1, Ep2, and Ep4 was captured
288 by the simulation. Interestingly, the NAQPMS underestimated the sulfate concentration
289 in Beijing during Ep2 and Ep4, but the nitrate and ammoniate concentrations during
290 these two episodes were successfully reproduced. This was related to the transport of
291 mineral dust (Ep2) and local emissions (Ep4). As discussed in the last paragraph,
292 Beijing had high mineral loadings for Ep2, which provided a favorable medium for
293 chemical transformation of anthropogenic SO₂ into sulfate in the form of CaSO₄ or
294 MgSO₄ (Wang et al., 2018b; Wang et al., 2017c). Underestimation of the sulfate
295 concentration for Ep4 may have been caused by local emissions in Beijing. As
296 illustrated in Fig. 3, the simulation failed to reproduce the sharp increase in both sulfate
297 and BC in Beijing during this episode. This is different from the case of Ep2, in which
298 sulfate was underestimated but BC was favorably reproduced. Wang et al. (2009) and
299 Ma et al. (2015) found that sulfate accounted for 40% and 6.6% of primary PM_{2.5}
300 emissions from industry and power plants, which also emit a large amount of BC. This
301 sharp increase in BC was a local-scale episode. In Langfang, a site 50–60 km from
302 Beijing, both the observed and simulated BC concentration increased slowly to 20 μg
303 m⁻³, which is much less than that in Beijing (45 μg m⁻³). The monthly emissions
304 employed in this study made it difficult to capture these short-term local-scale emission
305 changes. The simulated SO₂ concentrations are compared with the observations in Fig.
306 S2, and the normalized mean bias (NMBs) were less than 40%.

307 The number size distribution is critical to examining aerosol evolution during haze
308 episodes (Ma et al., 2017). In this study, both the simulation and observation revealed
309 a rapid increase in the GMD from 50 to approximately 120 nm during the initial stages
310 of episodes in Beijing (Fig. 4). The observed mean number concentration of aerosols
311 (dN/dlogDp) showed a unimodal distribution and was mainly concentrated in the
312 Aitken mode (25–100 nm) and accumulation mode (100–1,000 nm). The highest

313 concentration was approximately $1.8 \times 10^4 \text{ cm}^{-3}$ at a 100-nm diameter. These patterns
314 were favorably reproduced by the simulation. The simulated number concentrations
315 were underestimated in 10–60 nm by 20%–30% and overestimated in 80–150 nm by
316 20%. This indicated that the model needs to be improved regarding its treatment of new
317 particle formation and the volatility of primary organic aerosols.

318 Herein, the mass ratio of coating to BC (R_{BC}) was used as an indicator of aging
319 degree, which has been widely used in previous studies (Oshima et al., 2009; Collier et
320 al., 2018). Figure 11 shows that the mean simulated R_{BC} in Beijing was 4.5 and 5.0 in
321 the entire study period and during pollution episodes, respectively, which are extremely
322 close to the observations (~ 5.0 and 5.1) (Wang et al., 2018a). The high performance of
323 the model in terms of mass and number concentrations, compositions, and the aging
324 degree of aerosols gives us confidence for analyzing aerosol evolution during transport
325 in the megacity cluster centered on Beijing.

326 **3.2 Meteorology**

327 The simulated wind direction and speed coincided with the observations for the
328 haze episodes. In particular, the model captured low wind speeds, and the moments
329 when the wind shifted direction were well reproduced (Fig. S3). Regarding relative
330 humidity and temperature, WRF performed high values of R (0.68–0.93) and low
331 NMBs (-0.51 to 0.44) (Table S1). In particular, the high relative humidity during Ep1
332 was well reproduced. Inversion layers were present during the initial stage of haze
333 formation (Fig. S4). The height of the inversion layers varied among episodes. During
334 Ep1 and Ep6, strongly elevated inversion layers were present between 1 and 2 km,
335 whereas the inversion layers were close to the surface during other episodes.
336 Temperature inversion is favorable for pollution accumulation, and the model
337 reproduced this feature favorably. In sum, the high performance of the meteorological
338 simulation gave us confidence for $PM_{2.5}$ simulation.

339 **4 Results and discussion**

340 **4.1 Source apportionment of surface PM_{2.5}**

341 The simulated spatial distribution of average surface PM_{2.5} levels and the wind
342 vector during the six haze episodes are shown in Fig. 5. In general, two types of patterns
343 were observed. The first pattern corresponded to Ep1, Ep4, and Ep6 and reflected that
344 a highly polluted belt with PM_{2.5} over 200 $\mu\text{g m}^{-3}$ extended from the southwest to the
345 northeast along the Taihang mountain range. In the second pattern (Ep2, Ep3, and Ep5),
346 the PM_{2.5} level of 150–200 $\mu\text{g m}^{-3}$ was concentrated in three northern cities (Beijing,
347 Tianjin, and Tangshan). In the other cities, the PM_{2.5} mass concentrations ranged from
348 75 $\mu\text{g m}^{-3}$ to 115 $\mu\text{g m}^{-3}$, indicating a light pollution level according to the Technical
349 Regulation on Ambient Air Quality Index (on trial).

350 Figure 6 shows the contributions of regional transport and local emissions to
351 average PM_{2.5}, primary inorganic aerosol (PIA, including BC and inorganic primary
352 PM_{2.5}), and SIA levels in different cities during the study period. The contribution of
353 local emissions was more than that of regional transport to the PM_{2.5} mass concentration
354 in all cities, except Heng Shui, Cangzhou, Langfang, and Qinhuangdao; the magnitude
355 of local emission contributions was 49%–80%. The principle reason for this was the
356 accumulation of local PIA emissions. In most cities, 64%–93% of PIA originated from
357 local emissions (Fig. 6c). In contrast to PIA, the SIA contribution was dominated by
358 regional transport of emissions in other cities (50%–87%). Even the emissions of cities
359 outside the city cluster (e.g., Henan, Shanxi and Shandong) were transported to the
360 megacity cluster, travelling 500–1,000 km. In Beijing, the local contribution to total
361 PM_{2.5} and PIA was 74% and 94%, respectively, whereas regional transport from other
362 cities was the major source of SIA, contributing 51%. The difference in source
363 apportionment between PIA and SIA was related to the emission of PIA and formation
364 mechanisms of SIA. Regarding PIA, the inversion layer and weak winds during stable
365 weather conditions prevented PIA transport and resulted in local-scale accumulation of
366 PIA emissions. The regional transport provided sufficient time (1–3 days) and aerosol

367 surface for chemical transformation of precursors to SIA (Li et al., 2015; Li et al.,
368 2017b). This also indicates that regional controls on precursors would be the most
369 efficient way to decreasing the SIA concentration in this megacity cluster. Our results
370 agree favorably with the observed impact of regional emission controls in Asia-Pacific
371 Economic Cooperation China 2014. During this gathering, the SIA concentration in
372 Beijing decreased to a greater degree than the PIA concentration because of regional
373 controls (Sun et al., 2016).

374 The source apportionment in haze episodes in Beijing is illustrated in Fig. 7.
375 Regional transport contributed 14%–31% to the surface PM_{2.5} mass concentration
376 during the six episodes. The highest contribution of regional transport occurred in Ep1
377 and Ep5 (29% and 31% of the total PM_{2.5}, respectively). In Ep1 and Ep5, the
378 contribution of the SIA originating from regional transport reached 53% and 63%,
379 respectively. Interestingly, the regionally transported SIA had different source regions
380 in Ep1 and Ep5. In Ep5, SX, WHB, and NHB were the dominant source regions,
381 whereas the source regions for Ep1 were more diverse. This indicates the complexity
382 of regional transport in this megacity cluster. Compared with the episodes in November
383 2015, the effects of regional transport of PM_{2.5} and SIA mass concentrations were
384 weaker in this study, which may be related to the weather system and emission controls
385 in 2016 (Li et al., 2017b). Therefore, more studies on regional transport should be
386 conducted to further understand regional haze formation mechanisms. In other episodes
387 (Ep2, Ep3, Ep4, and Ep6), regional transport of surface PM_{2.5}, PIA, OM (organic
388 matters, sum of primary organic aerosols [POA] and secondary organic aerosols
389 [SOA]), and SIA mass concentrations were in the range 14%–23%, 3%–12%, 3%–14%,
390 and 30%–51%, respectively. Back trajectories and emissions source regions can be
391 connected (Fig. S5). Taking Ep6 for example, air mass mainly came from Shandong,
392 through SHB, WHB and finally arrived at Beijing. What's more, the height of trajectory
393 within WHB is low, so contribution of WHB should be big, which agreed with results
394 of Figure 7b, and source apportionment results showed that WHB contributed 24% to
395 SIA at Beijing during Ep6.

396 Figure 8 presents the relative contribution of regionally transported SIA and
397 variation of wind direction under different pollution levels in Beijing. The source
398 regions varied considerably under different pollution levels. When Beijing is controlled
399 by strong northerly wind, NHB and SX are the main source regions, contributing up to
400 30% and 19% to SIA, resulting in clean conditions ($SIA < 50 \mu\text{g m}^{-3}$). When Beijing is
401 mainly affected by southerly wind (southeast, south and southwest), WHB, EHB and
402 SD become the main source regions, contributing 27%, 13% and 15% to SIA,
403 respectively. Strong emissions of source regions lead to heavier pollution level in
404 Beijing. When Beijing is dominated by weak southeast wind, contribution from far
405 regions like HN and SD increases. Continuous transport and accumulation lead to
406 severe pollution ($SIA > 150 \mu\text{g m}^{-3}$). This indicates that wider regional emission control
407 is necessary to reduce severe pollution.

408 **4.2 Impact of regional transport of sulfate and its precursors** 409 **on Beijing**

410 Quantifying the impact of regional transport of sulfate and its precursors is a crucial
411 task. Sun et al. (2014) considered sulfate formed outside Beijing as regionally
412 transported sulfate, and they estimated that its contribution reached 75% during winter
413 haze episodes. By tagging emissions regions of precursors in models and ignoring
414 where secondary aerosols were formed, Li et al. (2017) and Timmermans et al. (2017)
415 estimated the contribution of transport to be 40%–50%. These estimated contributions
416 of regional transport are different in physical meaning, which may confuse
417 policymakers. In this study, we divided the sulfate mass concentration in Beijing into
418 four parts, LC, LTC, RLC, and RTC as described in Sect. 2.1. The regional transport
419 defined by Sun et al. (2014) was $LTC + RLC + RTC$, whereas in the studies by Li et al.
420 (2017) and Timmermans et al. (2017), it was $RLC + RTC$. In this study, we employed
421 $RLC + RTC$ as regional transport.

422 Figure 9a shows the contributions of LC, LTC, RLC, and RTC to the daily average
423 sulfate concentration in Beijing during the study period. RTC and LC were the

424 dominant sources of sulfate, contributing 71%–89% in total. The contributions of RTC
425 ranged from 29% in Ep6 to 59% in Ep2, and contributions of LC were 30%–42%. RTC
426 dominated the regional transport over the whole period, which indicates that chemical
427 conversions in the transport pathway of SO₂ were critical to haze formation. Notably,
428 the LTC contribution was comparable with that of LC in Ep3, Ep4, and Ep6. This
429 suggests that the SO₂ emitted in Beijing was blown away and formed sulfate outside
430 Beijing. And recirculation of air masses can be supported by HYSPLIT trajectories (Fig.
431 S6). Take trajectories at 23:00 on December 12 [LST] for example, air masses were
432 blown away Beijing by southwesterly, through Chengde, Tianjin and Langfang, and
433 finally travelled back to Beijing. These formed sulfates may have been blown back to
434 Beijing under certain weather conditions and were previously considered regional
435 transport. The contribution of LTC also largely explains the difference in estimated
436 regional transport contributions between Sun et al. (2014) and Li et al. (2017). In the
437 present study, LTC + RLC + RTC accounted for 58%–70% of the sulfate concentration
438 in the six episodes, which is relatively similar to the estimation (75%) of Sun et al.
439 (2014), which was based on the observed hourly increase rate of local sulfate
440 concentration.

441 In the initial and subsequent pollution stages, LC, LTC, and RTC showed different
442 patterns in Beijing. In Ep1, local contributions dominated before the sulfate
443 concentration increased rapidly (November 15 and 16). In particular, sulfate blown
444 back to Beijing from its local emissions (LTC) made a larger contribution (35%) than
445 RTC (25%). In the rapid rising phase of sulfate (November 17 and 18), contribution of
446 RTC increased from 25% to 47%. LC was also significant and contribution increased
447 considerably from 37% to 41%. These two parts (LC and RTC) explained the rapid
448 formation of sulfate in Beijing. This suggests that the joint control of local and regional
449 SO₂ emissions is essential for preventing the rapid formation of haze in this region,
450 which is receiving considerable attention and eliciting widespread interest among the
451 researchers and policymakers (Sun et al., 2014; Ma et al., 2017; Li et al., 2017b). This
452 feature is also reflected in Fig. 9b. Under clear conditions (sulfate < 20 μg m⁻³), the

453 local contributions (LC and LTC) were positively correlated with the sulfate mass
454 concentration. In total, they contributed 40%–60% of the sulfate mass concentration.
455 The ratio of LC to LTC was approximately 2:1. Under moderate sulfate levels ($20 \mu\text{g}$
456 $\text{m}^{-3} < \text{sulfate} < 35 \mu\text{g m}^{-3}$), the local contribution was lower—particularly the LTC—
457 leading to a ratio of LC to LTC of approximately 8. Contribution of sulfate formed in
458 the regional transport pathway (RTC) significantly increased from 40% to 65%. Under
459 heavy pollution levels ($> 35 \mu\text{g m}^{-3}$), the LC contributed up to 50% due to extremely
460 stable boundary layers. Our results are consistent with those of Ma et al. (2017), in
461 which regional transport and local heterogeneous chemistry were qualitatively
462 discovered to make high contributions to initial and subsequent pollution stages.

463 **4.3 Evolution of aerosol properties in Beijing during haze** 464 **episodes**

465 Aerosol properties such as the particle size and aging degree can change
466 dramatically on haze days because of fresh emissions, subsequent chemical conversions,
467 and regional transport, which strongly affect regional radiation and climate (Cappa et
468 al., 2012). As illustrated in Fig. 4b, the GMD of aerosols in Beijing increased
469 remarkably to approximately 120 nm during the six haze episodes, compared with 50
470 nm under clean conditions. Two stages were identified: an initial rising stage and a
471 sustained increase stage. In the initial stage, the GMD of aerosols increased by 50–60
472 nm within several hours, and the GMD then remained at 100–120 nm for several days
473 in the subsequent elevated pollution stage. This GMD increase during the initial stage
474 was mainly caused by the increase of accumulation-mode particles with diameters of
475 100–1,000 nm and Aitken-mode particles (Fig. 10). Under clean conditions ($\text{SIA} < 50$
476 $\mu\text{g m}^{-3}$), the average contributions of the three modes (nucleation, Aitken, and
477 accumulation modes) to the number concentration were comparable, although the
478 number of nucleation-mode particles decreased with SIA concentration. Under light-
479 moderate pollution conditions ($50 < \text{SIA} < 150 \mu\text{g m}^{-3}$), the proportion of accumulation-
480 mode particles significantly increased from 35% to 60%, whereas the proportion of

481 Aitken-mode particles slowly decreased. As discussed in previous sections, regional
482 transport played a dominant role during the initial stage. This indicates that
483 condensation, coagulation, and chemical transformation in the transport pathway
484 increased the number of particles with a diameter range of 100–1,000 nm. Finally, the
485 contributions of Aitken-mode and accumulation-mode particles remained stable under
486 the heavy-pollution conditions ($\text{SIA} > 150 \mu\text{g m}^{-3}$).

487 Aging processes play a critical role in the growth of particles during haze episodes.
488 According to observations, a significant coating of secondary components on BC was
489 found in the study period (Wang et al., 2018a). Figure 11 presents a time series of the
490 simulated R_{BC} , which is a favorable indicator of the aging degree (Oshima et al., 2009;
491 Collier et al., 2018). Higher R_{BC} indicates that BC had undergone more ageing. In this
492 study, the simulated R_{BC} was 2–10, with an average value of 4.5. Under pollution
493 conditions, R_{BC} was higher than that under clean conditions, with an average value of
494 5.0. R_{BC} in Beijing even exceeded 10.0 in some extremely severe pollution events,
495 which is close to observations of remote sites (Wang et al., 2017a; Massoli et al., 2015)
496 and aged particles (Cappa et al., 2012). Urban aerosols usually have a lower R_{BC}
497 because of fresh emissions and high R_{BC} in this study indicates that Beijing aerosol
498 particles were more aged during the haze episodes. On clean days, R_{BC} ranged from 2
499 to 5, with an average of 2.8. This is similar to the R_{BC} of vehicle emissions (< 3) (Liu
500 et al., 2017), indicating that Beijing is affected by local emission. Vehicle emissions
501 contributed 70% of BC in downtown Beijing in 2016 after strict controls on coal
502 burning had been implemented (Kebin He, personal communication).

503 Figure 12 shows the evolution of R_{BC} , GMD, and region source of BC along the
504 transport pathway from the source region to Beijing during the six haze episodes.
505 Aerosol properties including number concentration along transport per six hours are
506 shown in Table S2. The transport pathway was calculated using the HYSPLIT model.
507 The figure clearly shows that the aerosol properties changed considerably along the
508 transport pathway. In Ep1, the GMD of aerosols was only 97 nm at the initial site of the
509 24 h back trajectories (T-24). At a larger transport distance, the diameters of aerosol

510 particles were markedly increased to 128 nm in the middle (T₋₁₂) and 134 nm at the
511 final site (T₀) of the back trajectory. R_{BC} increased from 3.6 at T₋₂₄ to 8.7 at Beijing (T₀)
512 because of BC being coated during the transport. This indicates that BC underwent
513 considerable aging and increased in size while moving along the transport pathway.
514 Similar characteristics were discovered for Ep3–6. In Ep3, Ep4, Ep5, and Ep6, the
515 GMD in Beijing (T₀) was 126, 117, 124, and 116 nm, respectively, compared with 96,
516 95, 99, and 111 nm in the middle point of transport (T₋₁₂). R_{BC} also increased to 4.6–7.6.
517 An exception was Ep2, in which the GMD (106 nm) and R_{BC} (3.8) at the final ending
518 site (Beijing, T₀) were lower than those 6 h previously (T₋₆). Regional transport
519 contributed 95% of BC at T₋₆, whereas local emissions accounted for 87% of BC at T₀.
520 The number concentration was smaller at T₋₆ than that at T₀. Therefore, we conclude
521 that regional transport of aged aerosols led to a high GMD at T₋₆, and that the addition
522 of locally emitted fresh air caused a high number concentration but low GMD at T₀. In
523 clean areas, such as at T₋₂₄ in Ep5, R_{BC} was higher than 10 and the GMD was
524 considerably smaller.

525 **4.4 Impact of heterogeneous chemistry on sulfate mass** 526 **concentration**

527 Current models generally account for a part of the observed SO₄²⁻ concentrations
528 in China (Wang et al., 2014a). Heterogeneous chemistry on aerosol surfaces under high
529 relative humidity has been considered a potential missing source of sulfate formation
530 (Cheng et al., 2016; Zheng et al., 2015; Li et al., 2017a; Tang et al., 2016b). Li et al.
531 (2018) developed a simple parameterization of heterogeneous chemistry and
532 discovered that SO₂ uptake on aerosols partly closed the gap between simulation and
533 observation. In their study, uptake coefficients were dependent on the aerosol core and
534 shell species, shell thickness, and amount of aerosol liquid water. Zheng et al. (2013)
535 and Yang et al. (2014) measured local source profiles, and they reported that primary
536 sulfate from industry and power plants accounted for a large fraction of PIA.
537 Researchers also found that household coal burning can emit certain amounts of sulfate

538 (Zhang et al., 2018).

539 In this study, we examined the contributions of gas ($\text{SO}_2 + \text{OH}$) and aqueous
540 chemistry, heterogeneous chemistry, and primary sulfate emissions to the sulfate mass
541 concentration in Beijing (Fig. 13). In Ep1, under high relative humidity, the contribution
542 of heterogeneous chemistry was 33%. Primary emissions exerted an effect mostly under
543 light to moderate pollution levels (sulfate $< 20 \mu\text{g m}^{-3}$), whereas heterogeneous
544 chemistry played a crucial role under high pollution levels (sulfate $> 30 \mu\text{g m}^{-3}$). The
545 contributions of gas and aqueous chemistry were largely consistent under all pollution
546 conditions ($\sim 30\%$). This indicates that high relative humidity and aerosol loading
547 accelerated the SO_2 chemical transformation. Interestingly, the contribution of
548 heterogeneous chemistry was markedly higher when the sulfate mass concentration
549 exceeded the threshold of $20 \mu\text{g m}^{-3}$. Under high relative humidity and mass
550 concentration conditions, a higher aerosol surface area resulting from hygroscopic
551 growth and haze particles under high RH (60–80%) with aqueous shell due to phase
552 transition provided a favorable media for heterogeneous reactions (Tie et al., 2017; Sun
553 et al., 2018). The aforementioned threshold is relatively similar to that during the haze
554 episodes in the winter of 2013 (Li et al, 2018). For policymakers, implementing
555 measures to prevent the sulfate concentration from exceeding this threshold is essential.
556 Such measures would be effective for avoiding extremely high sulfate levels. In other
557 episodes, heterogeneous chemistry was depressed because of the low relative humidity
558 ($< 70\%$). Gas and aqueous chemistry and primary emissions contributed 35%–40% and
559 58%–61%, respectively. It should be noted that failure of the model to simulate mineral
560 dust led to underestimation of the sulfate level in Ep2. The interaction between SO_2 and
561 alkaline dust can contribute considerably to the sulfate concentration.

562 **5 Conclusions**

563 The contributions of regional transport to haze episodes over a megacity cluster
564 centered on Beijing have been under debate in recent decades. Investigating the

565 evolution of aerosol properties along the transport pathway may provide more
566 information on how researchers can improve the accuracy of regional transport and
567 chemistry impact assessments. To address one of the aims of the APHH 2016 winter
568 campaign, we employed a Eulerian chemical transport model (NAQPMS) and a
569 Lagrangian trajectory model (HYSPLIT) to assess the evolution of aerosols—in terms
570 of the number concentration, size distribution, and aging degree—in Beijing during six
571 haze episodes between November 15 and December 15, 2016. The transport of sulfate
572 and its precursors was also quantitatively investigated.

573 The results demonstrated that regional transport contributed 14%–31% to the
574 surface $PM_{2.5}$ mass concentration in Beijing during the six episodes, with a monthly
575 average contribution of 26%. Regarding aerosol components, 30%–62% of the SIA in
576 Beijing were regionally transported, whereas few PIAs ($< 10\%$) were contributed by
577 emissions from other regions. Source regions differed between episodes. During high-
578 pollution periods, WHB, SD, and EHB were the main source regions of SIA regionally
579 transported to Beijing, whereas NHB and SX made greater contributions under clean
580 and light pollution conditions. This indicates the complexity of regional transport in
581 this megacity cluster.

582 The chemical transformation of SO_2 along the transport pathway from source
583 regions except Beijing to Beijing (RTC) was the major source of SO_4^{2-} regional
584 transport and was more critical than the transport of sulfate formed in source regions
585 except Beijing (RLC). Compared with sulfate that was chemically transformed from
586 Beijing-emitted SO_2 and then blown back to Beijing (LTC), contribution of sulfate
587 produced in Beijing from Beijing-emitted SO_2 (LC) was generally greater. However,
588 RTC markedly increased in some episodes, and it explained the rapid formation of
589 sulfate in Beijing. This suggests that the joint control of local and regional SO_2
590 emissions is essential for reducing the rapid formation of haze in this region.

591 Aerosols became considerably aged during transport in haze episodes, which
592 altered R_{BC} and the size distribution of number concentrations. During haze episodes,

593 the GMD increased from less than 100 nm at the initial site to approximately 120 nm
594 at the final site (Beijing), and R_{BC} increased from 2–4 to 4–8. The number of
595 accumulation-mode particles with a diameter range of 100–1,000 nm increased
596 considerably more than the number of particles of different modes. R_{BC} in Beijing
597 during the episodes was higher than that of other urban regions (Collier et al., 2018).
598 At high pollution levels, R_{BC} was close to that in remote regions (Wang et al., 2017a),
599 which indicates that BC in Beijing under pollution conditions was more aged and thus
600 more likely to affect radiation and circulation.

601 Contributions from different pathways to sulfate in Beijing were also examined. In
602 episodes with high humidity (Ep1), the average contributions of gas and aqueous
603 chemistry, heterogeneous chemistry, and primary sulfate were comparable. But their
604 relative contributions varied with pollution levels. Under light to moderate pollution
605 levels, primary emissions mostly had an effect. But under high pollution levels during
606 Ep1, heterogeneous chemistry played a relatively crucial role. In other episodes (Ep2,
607 Ep3, Ep4, Ep5, and Ep6), gas and aqueous chemistry and primary emissions contributed
608 35%–40% and 58%–61%, respectively.

609 **Author contributions.**

610 HD and JL designed the idea and experiments. HD performed all the model runs,
611 did the analysis and wrote the paper. JL prepared the emissions data and contributed to
612 the paper writing. ZW and XC contributed to the model development; YS, PF, JJJ and
613 JG provided observation data. YW contributed to data processing. All authors discussed
614 the paper.

615 **Acknowledgements:**

616 Many thanks to the anonymous reviewers for their helpful comments to improve our
617 manuscript. This work was supported by the Natural Science Foundation of China
618 (41571130034; 91544227; 91744203; 41225019; 41705108) and the Chinese Ministry
619 of Science and Technology (2018YFC0213205 and 2017YFC0212402).

620 **References**

- 621 Anderson, H. R., Atkinson, R., Balbus, J., Brauer, M., Chapman, R., Chowdhury, Z.: Outdoor Air
622 Pollution and Health in the Developing Countries of Asia: A Comprehensive Review, Special
623 Report 18, Health Effects Institute, Boston, Massachusetts, 2010.
- 624 Bian, Y. X., Zhao, C. S., Ma, N., Chen, J., and Xu, W. Y.: A study of aerosol liquid water content
625 based on hygroscopicity measurements at high relative humidity in the North China Plain,
626 *Atmospheric Chemistry and Physics*, 14, 6417-6426, 10.5194/acp-14-6417-2014, 2014.
- 627 Boylan, J. W., & Russell, A. G.: PM and light extinction model performance metrics, goals, and
628 criteria for three-dimensional air quality models, *Atmospheric Environment*, 40(26), 4946-
629 4959, <https://doi.org/10.1016/j.atmosenv.2005.09.087>, 2006.
- 630 Cao J.: *PM_{2.5} and environment*. Science Press, 2014.
- 631 Cappa, C. D., Onasch, T. B., Massoli, P., Worsnop, D. R., Bates, T. S., Cross, E. S., ... Zaveri, R.
632 A.: Radiative Absorption Enhancements Due to the Mixing State of Atmospheric Black Carbon,
633 *Science*, 337(6098), 1078–1081, <https://doi.org/10.1126/science.1223447>, 2012.
- 634 Chen, X., Li, X., Yuan, X., Zeng, G., Liang, J., Li, X., ... Chen, G.: Effects of human activities and
635 climate change on the reduction of visibility in Beijing over the past 36 years, *Environ Int*, 116,
636 92-100, <https://doi.org/10.1016/j.envint.2018.04.009>, 2018.
- 637 Chen, X., Wang, Z., Li, J., & Yu, F.: Development of a regional chemical transport model with size-
638 resolved aerosol microphysics and its application on aerosol number concentration simulation
639 over china, *Scientific Online Letters on the Atmosphere Sola*, 10, 83-87,
640 <https://doi.org/10.2151/sola.2014-017>, 2014.
- 641 Chen, X., Wang, Z., Yu, F., Pan, X., Li, J., & Ge, B., et al.: Estimation of atmospheric aging time of
642 black carbon particles in the polluted atmosphere over central-eastern china using
643 microphysical process analysis in regional chemical transport model. *Atmospheric*
644 *Environment*, 163, 44-56, <https://doi.org/10.1016/j.atmosenv.2017.05.016>, 2017.
- 645 Cheng, Y., Zheng, G., Wei, C., Mu, Q., Zheng, B., & Wang, Z., et al: Reactive nitrogen chemistry
646 in aerosol water as a source of sulfate during haze events in china, *Science Advances*, 2(12),
647 <https://doi.org/10.1126/sciadv.1601530>, 2016.
- 648 Collier, S., Williams, L. R., Onasch, T. B., Cappa, C. D., Zhang, X., & Russell, L. M., et al: Influence
649 of emissions and aqueous processing on particles containing black carbon in a polluted urban
650 environment: insights from a soot particle-aerosol mass spectrometer, *Journal of Geophysical*
651 *Research Atmospheres*, 123(12), 6648-6666, <https://doi.org/10.1002/2017jd027851>, 2018.
- 652 Draxler, R. R., & Hess, G. D: An overview of the HYSPLIT 4 modeling system for trajectories,
653 dispersion, and deposition, *Australian Meteorological Magazine*, 47(4), 295-308, 1998.
- 654 Du, W., Zhao, J., Wang, Y., Zhang, Y., Wang, Q., & Xu, W., et al: Simultaneous measurements of
655 particle number size distributions at ground level and 260 m on a meteorological tower in urban
656 Beijing, china, *Atmospheric Chemistry & Physics*, 17(11), 6797-6811,

657 <https://doi.org/10.5194/acp-17-6797-2017>, 2017.

658 Gao, J., Peng, X., Chen, G., Xu, J., Shi, G. L., Zhang, Y. C., and Feng, Y. C.: Insights into the
659 chemical characterization and sources of PM_{2.5} in Beijing at a 1-h time resolution, *The Science*
660 *of the total environment*, 542, 162-171, [10.1016/j.scitotenv.2015.10.082](https://doi.org/10.1016/j.scitotenv.2015.10.082), 2016.

661 Han, B., Zhang, R., Yang, W., Bai, Z., Ma, Z., & Zhang, W: Heavy haze episodes in Beijing during
662 January 2013: inorganic ion chemistry and source analysis using highly time-resolved
663 measurements from an urban site, *Science of the Total Environment*, 544, 319-329,
664 <https://doi.org/10.1016/j.scitotenv.2015.10.053>, 2016.

665 Huang, R. J., Zhang, Y., Bozzetti, C., Ho, K. F., Cao, J. J., Han, Y., . . . Prevot, A. S: High secondary
666 aerosol contribution to particulate pollution during haze events in China, *Nature*, 514(7521),
667 218-222, <https://doi.org/10.1038/nature13774>, 2014.

668 Hyslop, N. P.: Impaired visibility: the air pollution people see, *Atmospheric Environment*, 43(1),
669 182-195, <https://doi.org/10.1016/j.atmosenv.2008.09.067>, 2009.

670 Lee, A. K. Y., Chen, C. L., Liu, J., Price, D. J., Betha, R., Russell, L. M., Zhang, X., and Cappa, C.
671 D.: Formation of secondary organic aerosol coating on black carbon particles near vehicular
672 emissions, *Atmos. Chem. Phys.*, 17(24), 15055-15067, [https://doi.org/10.5194/acp-17-15055-](https://doi.org/10.5194/acp-17-15055-2017)
673 [2017](https://doi.org/10.5194/acp-17-15055-2017), 2017.

674 Li, G., Bei, N., Cao, J., Huang, R., Wu, J., & Feng, T., et al.: A possible pathway for rapid growth
675 of sulfate during haze days in china, *Atmospheric Chemistry & Physics*, 17(5), 3301-3316,
676 <https://doi.org/10.5194/acp-17-3301-2017>, 2017a.

677 Li, J., Chen, X., Wang, Z., Du, H., Yang, W., & Sun, Y., et al.: Radiative and heterogeneous chemical
678 effects of aerosols on ozone and inorganic aerosols over east Asia, *Science of the Total*
679 *Environment*, 622-623, 1327, <https://doi.org/10.1016/j.scitotenv.2017.12.041>, 2018.

680 Li, J., Du, H., Wang, Z., Sun, Y., Yang, W., & Li, J., et al.: Rapid formation of a severe regional
681 winter haze episode over a mega-city cluster on the North China Plain, *Environmental*
682 *Pollution*, 223, 605-615, <https://doi.org/10.1016/j.envpol.2017.01.063>, 2017b.

683 Li, J., Han, Z.: A modeling study of severe winter haze events in Beijing and its neighboring regions,
684 *Atmospheric Research*, 170, 87-97, <https://doi.org/10.1016/j.atmosres.2015.11.009>, 2016.

685 Li, J., Wang, Z., Huang, H., Min, H. U., Meng, F., & Sun, Y., et al.: Assessing the effects of trans-
686 boundary aerosol transport between various city clusters on regional haze episodes in spring
687 over east china, *Tellus*, 65(1), 60-73, <https://doi.org/10.3402/tellusb.v65i0.20052>, 2013.

688 Li, J., Yang, W., Wang, Z., Chen, H., Hu, B., & Li, J., et al.: A modeling study of source–receptor
689 relationships in atmospheric particulate matter over northeast Asia. *Atmospheric Environment*,
690 91(7), 40-51, <https://doi.org/10.1016/j.atmosenv.2014.03.027>, 2014.

691 Li, J., Wang, Z.F., Zhuang, G., Luo, G., Sun, Y., Wang, Q.: Mixing of Asian mineral dust with
692 anthropogenic pollutants over East Asia: a model cast study of a super-dust storm in March
693 2010. *Atmos. Chem. Phys.* 12 (16), 7591-7607. <https://dx.doi.org/10.5194/acp-12-7591-2012>,
694 2012.

- 695 Li, P., Yan, R., Yu, S., Wang, S., Liu, W., & Bao, H.: Reinstatement of regional transport of PM_{2.5} as a major
696 cause of severe haze in Beijing, *Proc Natl Acad Sci U S A*, 112(21), E2739-2740,
697 <https://doi.org/10.1073/pnas.1502596112>, 2015.
- 698 Liu, D., Whitehead, J., Alfarra, M. R., Reyes-villegas, E., Spracklen, D. V., & Reddington, C. L., et
699 al.: Black-carbon absorption enhancement in the atmosphere determined by particle mixing
700 state, *Nature Geoscience*, 10(3), 184-188, <https://doi.org/10.1038/ngeo2901>, 2017.
- 701 Liu, X., Zhang, Y., Jung, J., Gu, J., Li, Y., & Guo, S., et al.: Research on the hygroscopic properties
702 of aerosols by measurement and modeling during CAREBeijing-2006, *Journal of Geophysical
703 Research Atmospheres*, 114(16), 4723-4734, <https://doi.org/10.1029/2008jd010805>, 2009.
- 704 Ma, Q., Wu, Y., Zhang, D., Wang, X., Xia, Y., Liu, X., . . . Zhang, R.: Roles of regional transport
705 and heterogeneous reactions in the PM_{2.5} increase during winter haze episodes in Beijing, *Sci
706 Total Environ*, 599-600, 246-253, <https://doi.org/10.1016/j.scitotenv.2017.04.193>, 2017.
- 707 Ma, X., & Yu, F.: Seasonal variability of aerosol vertical profiles over east us and west Europe:
708 GEOS-Chem/APM simulation and comparison with CALIPSO observations, *Atmospheric
709 Research*, 140-141(31), 28-37, <https://doi.org/10.1016/j.atmosres.2014.01.001>, 2014.
- 710 Ma, Z., Liang YP, Zhang J.: PM_{2.5} profiles of typical sources in Beijing, *Acta Science
711 Circumstantiae*, 35(12), 4043-4052, <https://doi.org/10.13671/j.hjkxxb.2015.0584>, 2015.
- 712 Massoli, P., Onasch, T. B., Cappa, C. D., Nuumaan, I., Hakala, J., & Hayden, K., et al.:
713 Characterization of black carbon containing particles from soot particle aerosol mass
714 spectrometer measurements on the R/V Atlantis during CalNex 2010, *Journal of Geophysical
715 Research Atmospheres*, 120(6), 2575-2593, <https://doi.org/10.1002/2014jd022834>, 2015.
- 716 Morgan, W. T., Ouyang, B., Allan, J. D., Aruffo, E., Di Carlo, P., Kennedy, O. J., Lowe, D., Flynn,
717 M. J., Rosenberg, P. D., Williams, P. I., Jones, R., McFiggans, G. B., and Coe, H.: Influence of
718 aerosol chemical composition on N₂O₅ uptake: airborne regional measurements in
719 northwestern Europe, *Atmospheric Chemistry and Physics*, 15, 973-990, 10.5194/acp-15-973-
720 2015, 2015.
- 721 Nenes, A., Pandis, S.N., Pilinis, C.: ISORROPIA: A new thermodynamic equilibrium model for
722 multiphase multicomponent inorganic aerosols, *Aquat. Geochem.* 4(1), 123-152.
723 <https://dx.doi.org/10.1023/A:1009604003981>, 1998.
- 724 Oshima, N., Koike, M., Zhang, Y., Kondo, Y., Moteki, N., & Takegawa, N., et al.: Aging of black
725 carbon in outflow from anthropogenic sources using a mixing state resolved model: model
726 development and evaluation, *Journal of Geophysical Research Atmospheres*, 114(D6),
727 <https://doi.org/10.1029/2008jd010680>, 2009.
- 728 Pan, X., Ge, B., Wang Z., Tian, Y., et al.: Synergistic effect of water-soluble species and relative
729 humidity on morphological changes of aerosol particles in Beijing mega-city during severe
730 pollution episodes, *Atmos. Chem. Phys. Discuss*, 1-24, <https://doi.org/10.5194/acp-2018-623>,
731 2018.
- 732 Peng J, Hu M, Guo S, et al.: Markedly enhanced absorption and direct radiative forcing of black
733 carbon under polluted urban environments, *Proc Natl Acad Sci USA*, 113(16), 4266-4271,

- 734 <https://doi.org/10.1073/pnas.1602310113>, 2016.
- 735 Riemer, N., Vogel, H., Vogel, B., Anttila, T., Kiendler-Scharr, A., and Mentel, T. F.: Relative
736 importance of organic coatings for the heterogeneous hydrolysis of N₂O₅ during summer in
737 Europe, *Journal of Geophysical Research-Atmospheres*, 114(D17), 10.1029/2008jd011369,
738 2009.
- 739 Shi, Z., Vu, T., and Kotthaus, S.: Introduction to Special Issue-In-depth study of air pollution sources
740 and processes within Beijing and its surrounding region (APHH-Beijing), *Atmos. Chem. Phys.*
741 *Discuss.*, 10.5194/acp-2018-922, 2018.
- 742 Sun, Y., Chen, C., Zhang, Y., Xu, W., Zhou, L., Cheng, X., . . . Wang, Z.: Rapid formation and
743 evolution of an extreme haze episode in Northern China during winter 2015, *Sci Rep*, 6(1),
744 27151. <https://doi.org/10.1038/srep27151>, 2016.
- 745 Sun, Y., Du, W., Wang, Q., Zhang, Q., Chen, C., & Chen, Y., et al. Real-time characterization of
746 aerosol particle composition above the urban canopy in Beijing: insights into the interactions
747 between the atmospheric boundary layer and aerosol chemistry, *Environmental Science &*
748 *Technology*, 49(19), 11340-11347, <https://doi.org/10.1021/acs.est.5b02373>, 2015.
- 749 Sun, Y., Jiang, Q., Wang, Z., Fu, P., Li, J., Yang, T., & Yin, Y.: Investigation of the sources and
750 evolution processes of severe haze pollution in Beijing in January 2013, *Journal of Geophysical*
751 *Research: Atmospheres*, 119(7), 4380-4398, <https://doi.org/10.1002/2014jd021641>, 2014.
- 752 Tang, G., Zhang, J., Zhu, X., Song, T., Munkel, C., Hu, B., et al.: Mixing layer height and its
753 implications for air pollution over Beijing, China, *Atmos. Chem. Phys.*, 16(4), 2459-2475,
754 <https://doi.org/10.5194/acp-16-2459-2016>, 2016a.
- 755 Tang, M. J., Larish, W. A., Fang, Y., Gankanda, A., and Grassian, V. H.: Heterogeneous Reactions
756 of Acetic Acid with Oxide Minerals: Effects of Mineralogy and Relative Humidity, *J. Phys.*
757 *Chem. A*, 120(28), 5609-5616, <https://doi.org/10.1021/acs.jpca.6b05395>, 2016b.
- 758 Tie, X., Huang, R. J., Cao, J., Zhang, Q., Cheng, Y., Su, H., . . . O'Dowd, C. D.: Severe Pollution in
759 China Amplified by Atmospheric Moisture, *Sci Rep*, 7(1), [https://doi.org/10.1038/s41598-017-](https://doi.org/10.1038/s41598-017-15909-1)
760 15909-1, 2017.
- 761 Timmermans, R., Kranenburg, R., Manders, A., Hendriks, C., Segers, A., & Dammers, E., et al.:
762 Source apportionment of PM_{2.5} across china using LOTOS-EUROS, *Atmospheric*
763 *Environment*, 164, 370-386, <https://doi.org/10.1016/j.atmosenv.2017.06.003>, 2017.
- 764 Wang, J., Liu, D., Ge, X., Wu, Y., Shen, F., Chen, M., . . . Sun, Y.: Characterization of black carbon-
765 containing fine particles in Beijing during wintertime, *Atmospheric Chemistry and Physics*
766 *Discussions*, 1-25, <https://doi.org/10.5194/acp-2018-800>, 2018a.
- 767 Wang, J., Zhang, Q., Chen, M. D., Collier, S., Zhou, S., & Ge, X., et al.: First chemical
768 characterization of refractory black carbon aerosols and associated coatings over the Tibetan
769 plateau (4730 m a.s.l), *Environmental Science & Technology*, 51(24), 14072-14082,
770 <https://doi.org/10.1021/acs.est.7b03973>, 2017a.
- 771 Wang, S., Zhao, X., Li, X., Wei, W., Hao, J.: Study on fine particle emission characteristics of

- 772 industrial coal-fired chain furnace. *Environmental Science (Chines)*, 30 (4), 963-968,
773 <https://doi.org/10.3321/j.issn:0250-3301.2009.04.004>, 2009.
- 774 Wang, Y. Y., Liu, F. S., He, C. L., Bi, L., Cheng, T. H., Wang, Z. L., Zhang, H., Zhang, X. Y., Shi,
775 Z. B., and Li, W. J.: Fractal Dimensions and Mixing Structures of Soot Particles during
776 Atmospheric Processing, *Environ Sci Tech Let*, 4, 487-493, 10.1021/acs.estlett.7b00418,
777 2017b.
- 778 Wang, Y., Zhang, Q., Jiang, J., Zhou, W., Wang, B. Y., He, K. B., . . . Xie, Y. Y.: Enhanced sulfate
779 formation during china's severe winter haze episode in January 2013 missing from current
780 models, *Journal of Geophysical Research Atmospheres*, 119(17), 10425-10440,
781 <https://doi.org/doi:10.1002/2013jd021426>, 2014a.
- 782 Wang, Z., Maeda, T., Hayashi, M., Hsiao, L.F., Liu, K.Y.: A nested air quality prediction modeling
783 system for urban and regional scales, application for high-ozone episode in Taiwan, *Water, Air,
784 Soil Pollut*, 130, 391-396, <https://dx.doi.org/10.1023/A:1013833217916>. 2001.
- 785 Wang, Z., Jie, L., Wang, Z., Yang, W. Y., Tang, X., & Ge, B. Z., et al.: Modeling study of regional
786 severe hazes over mid-eastern China in January 2013 and its implications on pollution
787 prevention and control, *Science China Earth Sciences*, 57(1), 3-13,
788 <https://dx.doi.org/10.1007/s11430-013-4793-0>, 2014b.
- 789 Wang, Z., Pan, X., Uno, I., Li, J., Wang, Z., Chen, X., Fu, P., Yang, T., Kobayashi, H., Shimizu, A.,
790 Sugimoto, N., and Yamamoto, S.: Significant impacts of heterogeneous reactions on the
791 chemical composition and mixing state of dust particles: A case study during dust events over
792 northern China, *Atmospheric Environment*, 159, 83-91,
793 <https://doi.org/10.1016/j.atmosenv.2017.03.044>, 2017c.
- 794 Wang, Z., Pan, X., Uno, I., Chen, X., Yamamoto, S., Zheng, H., Li, J., and Wang, Z.: Importance of
795 mineral dust and anthropogenic pollutants mixing during a long-lasting high PM event over
796 East Asia, *Environmental pollution*, 234, 368-378,
797 <https://doi.org/10.1016/j.envpol.2017.11.068>, 2018b.
- 798 Wiedinmyer, C., Akagi, S. K., Yokelson, R. J., & Emmons, L. K.: The fire inventory from NCAR
799 (FINN) – a high resolution global model to estimate the emissions from open burning,
800 *Geoscientific Model Development*, 4(3), 625-641, <https://doi.org/10.5194/gmd-4-625-2011>,
801 2011.
- 802 Wu, J. B., Wang, Z., Wang, Q., Li, J., Xu, J., & Chen, H., et al.: Development of an on-line source-
803 tagged model for sulfate, nitrate and ammonium: A modeling study for highly polluted periods
804 in Shanghai, China. *Environmental Pollution*, 221, 168-179,
805 <https://doi.org/10.1016/j.envpol.2016.11.061>, 2017.
- 806 Xie, C., Xu, W., Wang, J., Wang, Q., Liu, D., Tang, G., Chen, P., Du, W., Zhao, J., Zhang, Y., Zhou,
807 W., Han, T., Bian, Q., Li, J., Fu, P., Wang, Z., Ge, X., Allan, J., Coe, H., and Sun, Y.: Vertical
808 characterization of aerosol optical properties and brown carbon in winter in urban Beijing,
809 China, *Atmospheric Chemistry and Physics Discussions*, 1-28, 10.5194/acp-2018-788, 2018.
- 810 Yang, H. H.: Filterable and condensable fine particulate emissions from stationary sources, *Aerosol*

811 & Air Quality Research, 14(7), 2010-2016, <https://doi.org/10.4209/aaqr.2014.08.0078>, 2014.

812 Yang, Y., Liu, X., Qu, Y., Wang, J., An, J., & Zhang, Y., et al.: Formation mechanism of continuous
813 extreme haze episodes in the megacity Beijing, China, in January 2013. Atmospheric Research,
814 155, 192-203, <https://doi.org/10.1016/j.atmosres.2014.11.023>, 2015.

815 Yang, Y., Wang, H., Smith, S. J., Easter, R., Ma, P. L., Qian, Y., . . . Rasch, P. J.: Global source
816 attribution of sulfate concentration and direct and indirect radiative forcing, Atmospheric
817 Chemistry and Physics, 17(14), 8903-8922, <https://doi.org/10.5194/acp-17-8903-2017>, 2017a.

818 Yang, Y., Wang, H., Smith, S. J., Ma, P.-L., & Rasch, P. J.: Source attribution of black carbon and
819 its direct radiative forcing in China, Atmospheric Chemistry and Physics, 17(6), 4319-4336,
820 <https://doi.org/10.5194/acp-17-4319-2017>, 2017b.

821 Ying, Q. Wu, L. Zhang, H.: Local and inter-regional contributions to PM_{2.5} nitrate and sulfate in
822 China, Atmos. Environ., 94, 582-592, <https://doi.org/10.1016/j.atmosenv.2014.05.078>, 2014.

823 Yu, F., & Luo, G.: Simulation of particle size distribution with a global aerosol model: contribution
824 of nucleation to aerosol and CCN number concentrations, Atmospheric Chemistry & Physics,
825 9(20), 7691-7710, <https://doi.org/10.5194/acp-9-7691-2009>, 2009.

826 Zhang, S. L., Ma, N., Kecorius, S., Wang, P. C., Hu, M., Wang, Z. B., Gross, J., Wu, Z. J., and
827 Wiedensohler, A.: Mixing state of atmospheric particles over the North China Plain,
828 Atmospheric Environment, 125, 152-164, [10.1016/j.atmosenv.2015.10.053](https://doi.org/10.1016/j.atmosenv.2015.10.053), 2016.

829 Zhang, Y., Yuan, Q., Huang, D., and Kong, S.: Direct Observations of Fine Primary Particles From
830 Residential Coal Burning: Insights Into Their Morphology, Composition, and Hygroscopicity,
831 Journal of Geophysical Research, 123, 12964–12979, 2018.

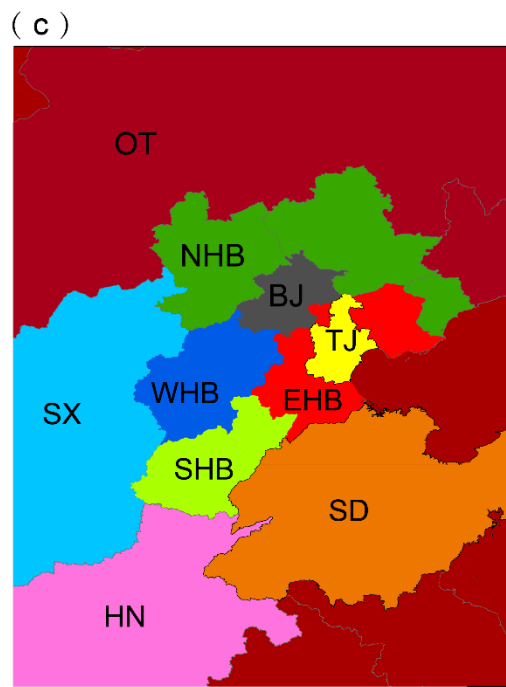
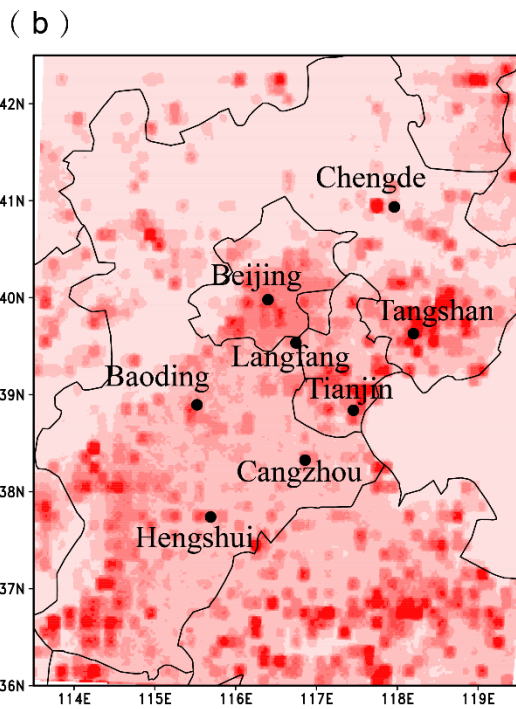
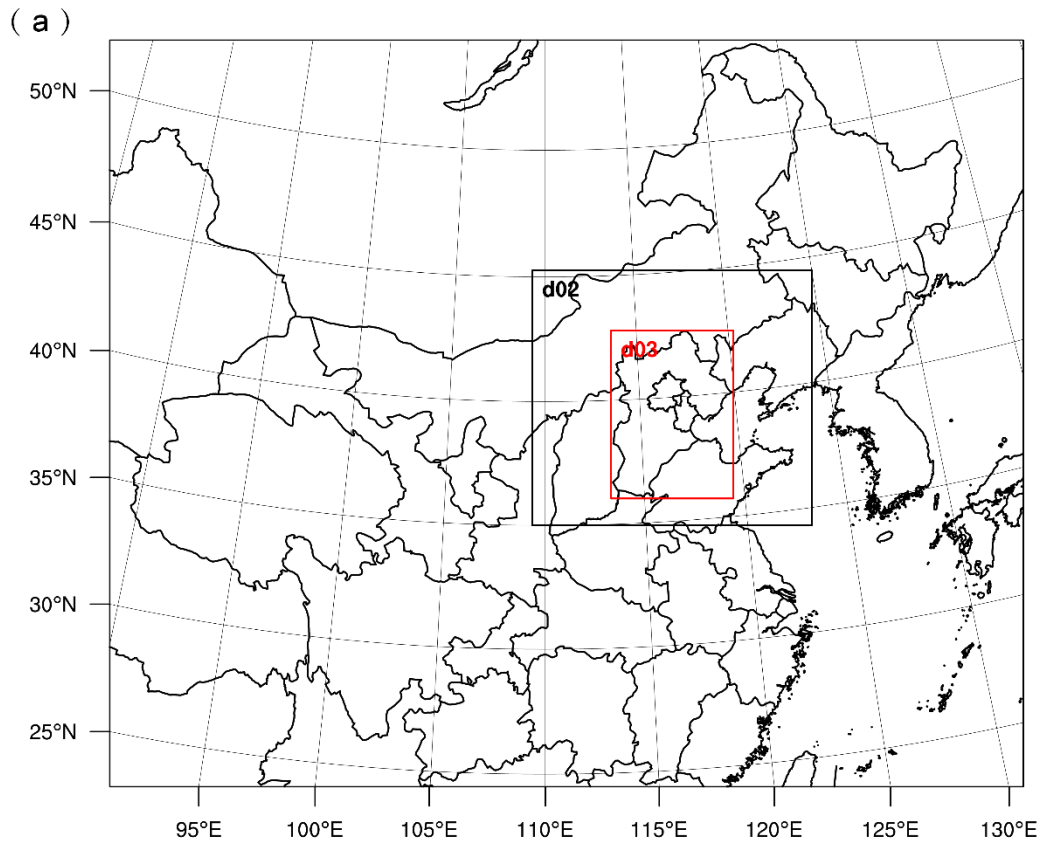
832 Zhao, X. J., Zhao, P. S., Xu, J., Meng, W., Pu, W. W., Dong, F., . . . Shi, Q. F.: Analysis of a winter
833 regional haze event and its formation mechanism in the North China Plain, Atmospheric
834 Chemistry and Physics, 13(11), 5685-5696, <https://doi.org/10.5194/acp-13-5685-2013>, 2013.

835 Zheng, B., Zhang, Q., Zhang, Y., He, K. B., Wang, K., Zheng, G. J., . . . Kimoto, T.: Heterogeneous
836 chemistry: a mechanism missing in current models to explain secondary inorganic aerosol
837 formation during the January 2013 haze episode in North China, Atmospheric Chemistry and
838 Physics, 15(4), 2031-2049, <https://doi.org/10.5194/acp-15-2031-2015>, 2015.

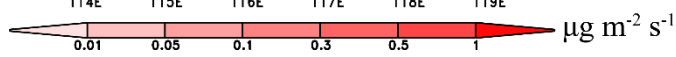
839 Zheng M., Zhang Y., Yan C., et al.: Establishment of PM_{2.5} industrial source profile in Shanghai,
840 China Environmental Science, 33(8), 1354-1359, <https://doi.org/10.3969/j.issn.1000-6923.2013.08.002>, 2013.

842 Zhu, X., Tang, G., Hu, B., Wang, L., Xin, J., & Zhang, J., et al.: Regional pollution and its formation
843 mechanism over north China plain: a case study with ceilometer observations and model
844 simulations, Journal of Geophysical Research Atmospheres, 121(24), 14574-14588,
845 <https://doi.org/10.1002/2016jd025730>, 2016.

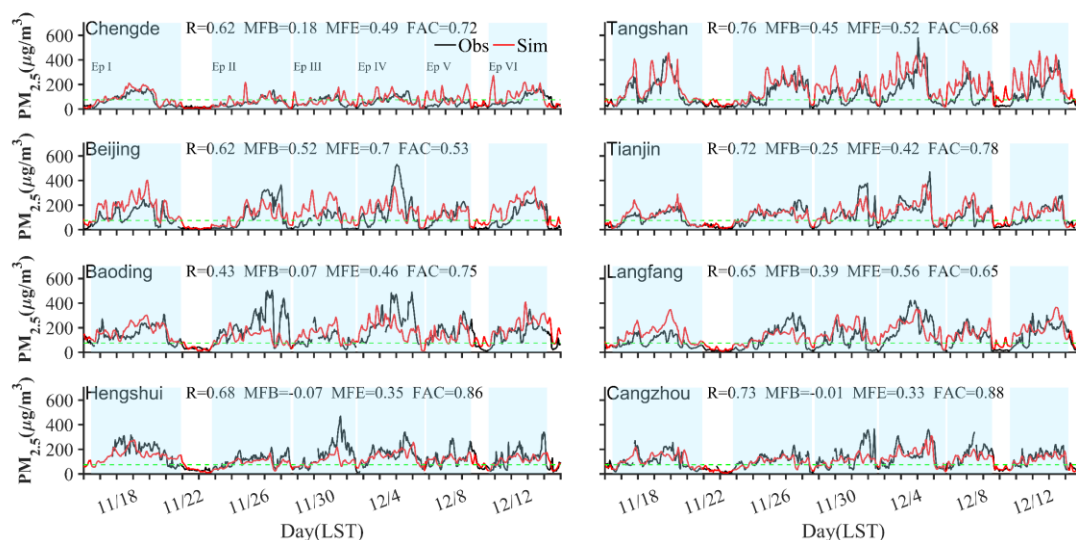
846 **Figures**



847

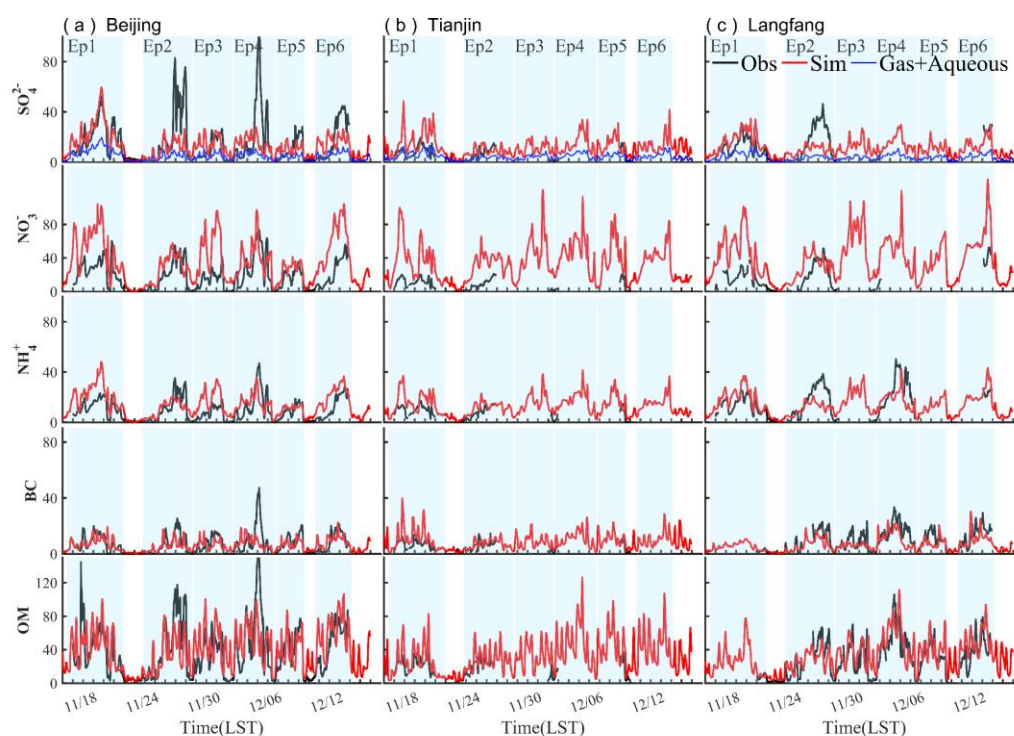


848 **Figure 1.** (a) Simulation domains. (b) Primary PM_{2.5} emission rates of the innermost
 849 domain and locations of observation sites (black dots). (c) tracer tagging regions which
 850 are described in Table 1.



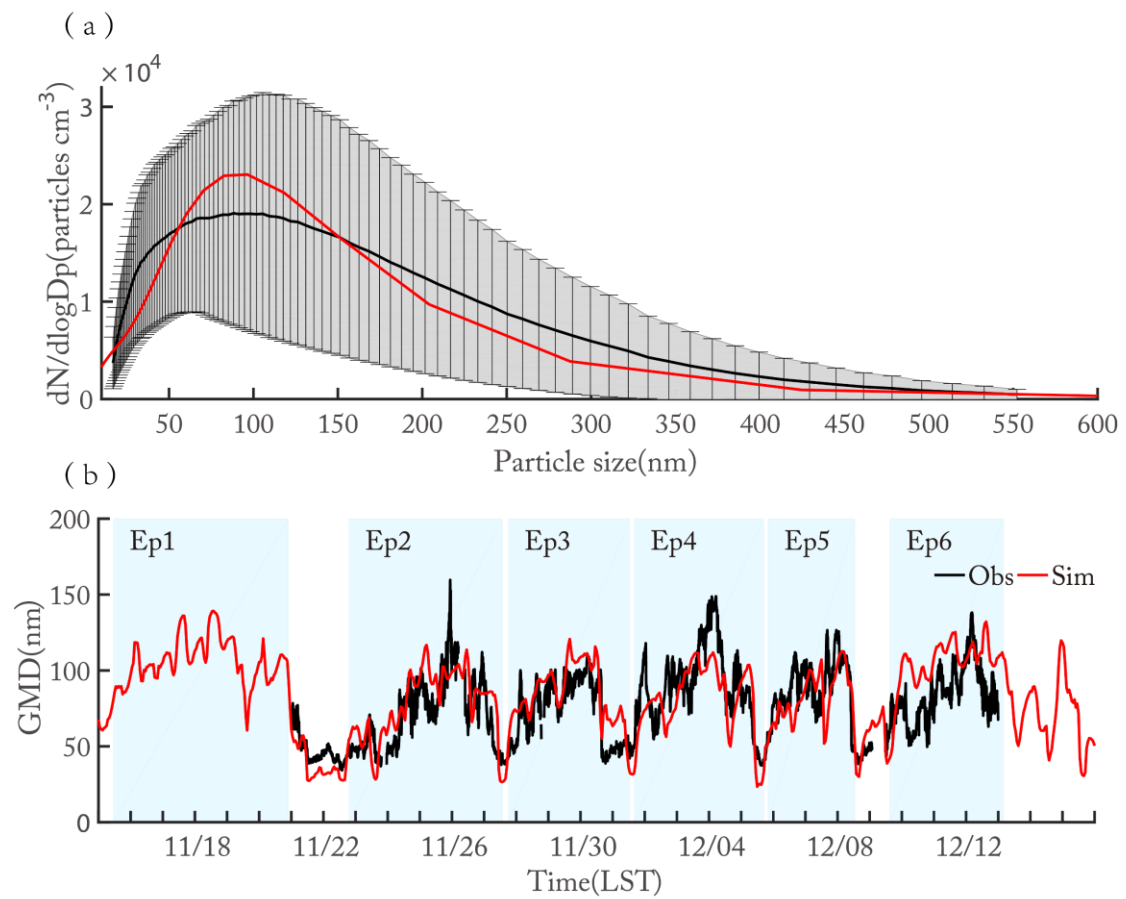
851

852 **Figure 2.** Comparison between the simulated and observed hourly concentrations of
 853 $PM_{2.5}$ for different sites. Black lines refer to observation and the red lines are simulation
 854 results; light blue shadows are six episodes identified; green lines mean $75 \mu g m^{-3}$, as a
 855 criterion judging whether pollution or not.



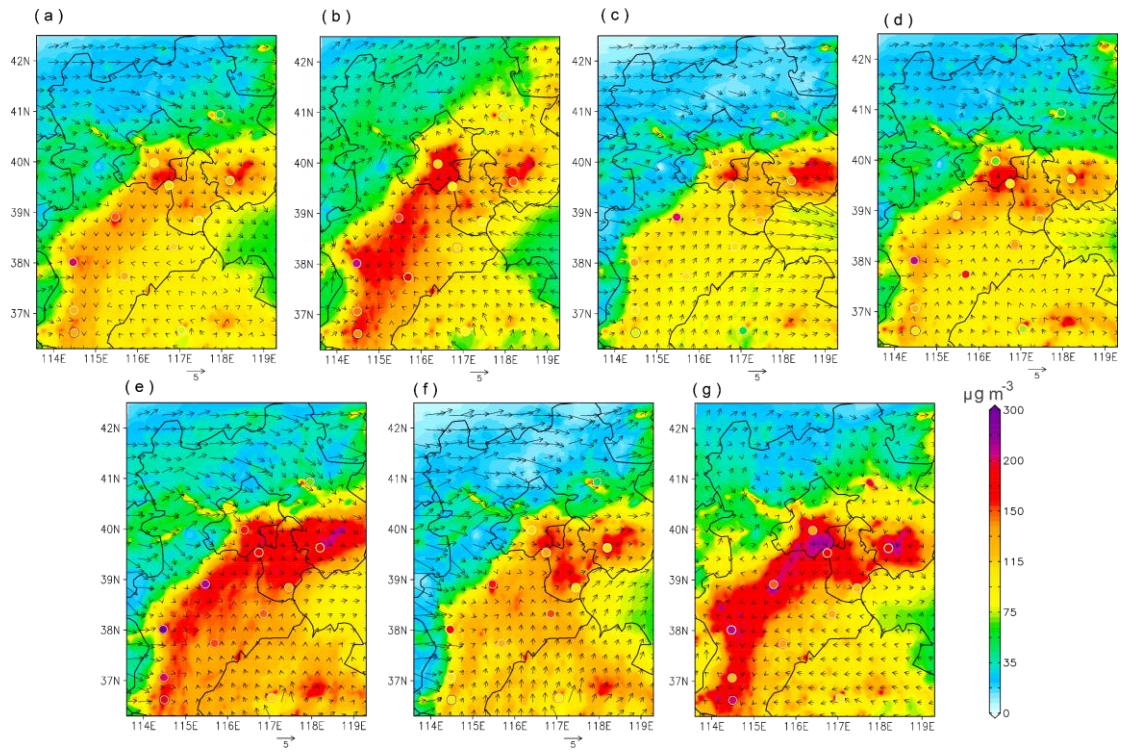
856

857 **Figure 3.** Comparison between the simulated (red) and observed (solid black) hourly
 858 components including sulfate, nitrate, ammonia, black carbon and organic aerosols at
 859 (a) Beijing, (b) Tianjin and (c) Langfang. Blue lines refer to sulfate produced by gas
 860 and aqueous chemistry reactions.



861

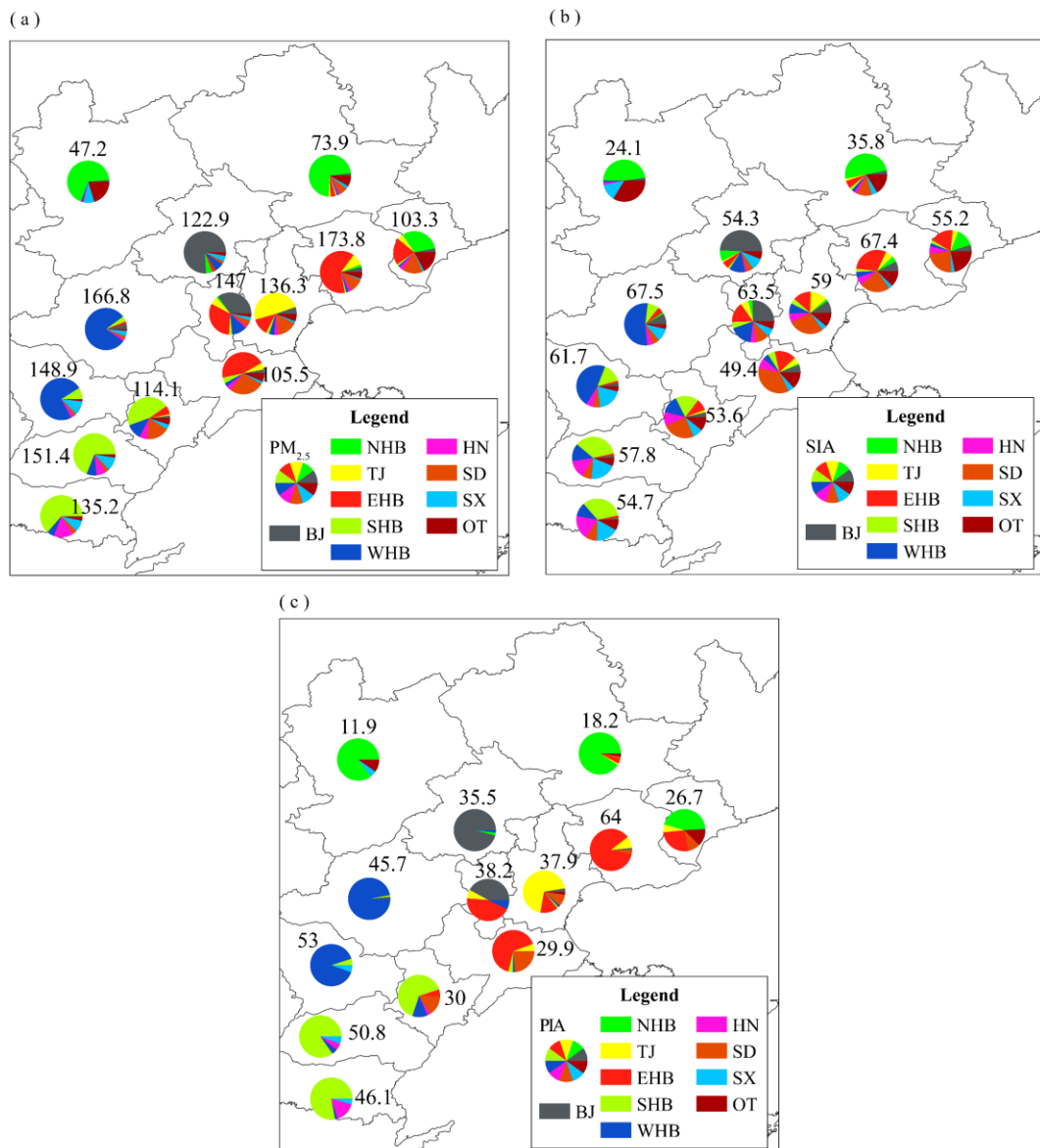
862 **Figure 4.** (a) Particle size distribution in Beijing at ground level. (b) Comparison of
 863 geometric mean diameter (GMD) for particles during range of 16–600nm between
 864 observation and simulation in Beijing. Black solid line and red solid line represent
 865 observation and simulation respectively.



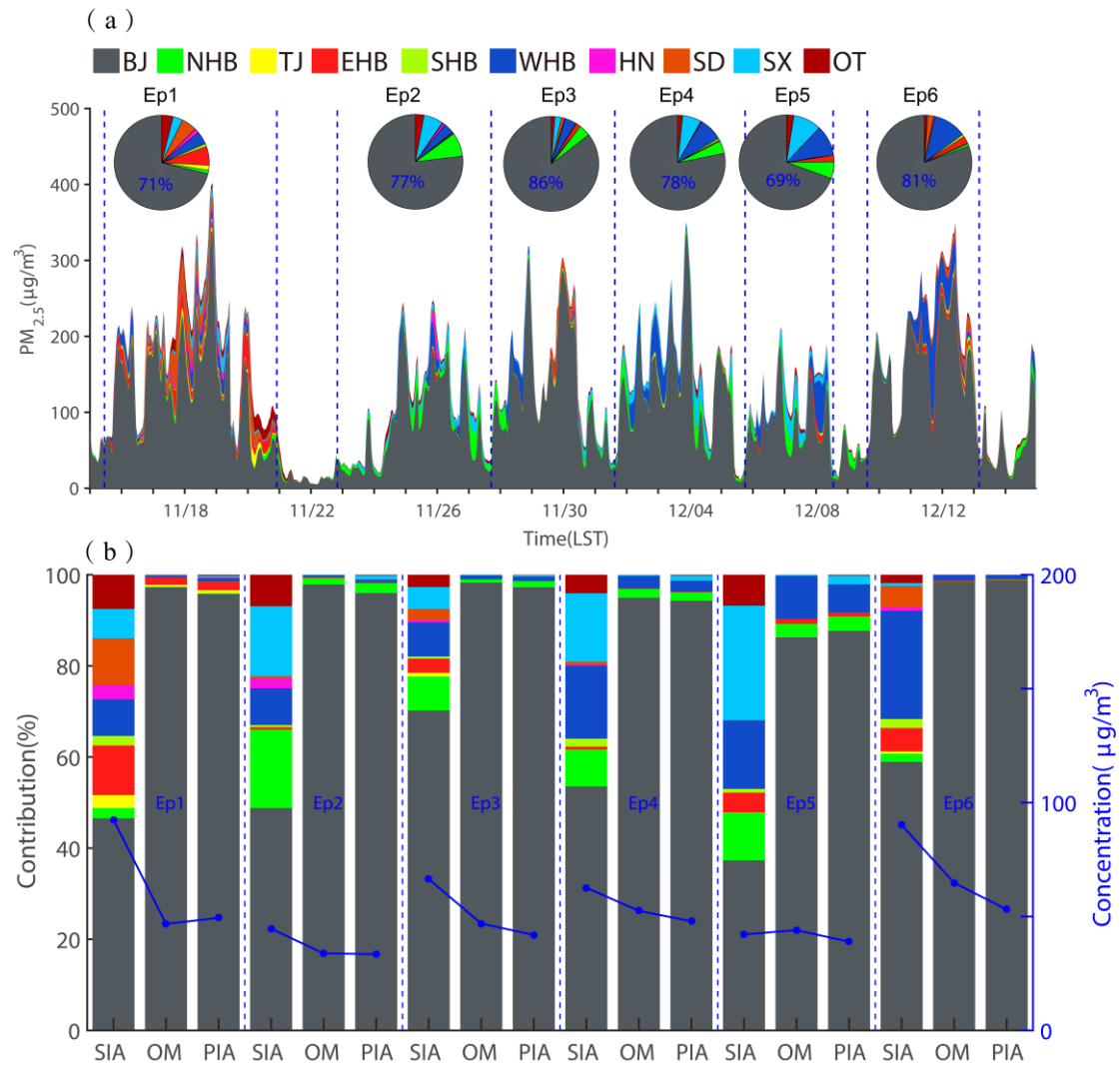
866

867 **Figure 5.** Spatial distribution of simulated average surface PM_{2.5} ($\mu\text{g m}^{-3}$) and wind (m
 868 s^{-1}) over BTH area. (a) average of the whole study period, (b)–(g) episode average of
 869 episode1–6 identified before. Solid circles represent observations with the same color
 870 bar with simulations.

871

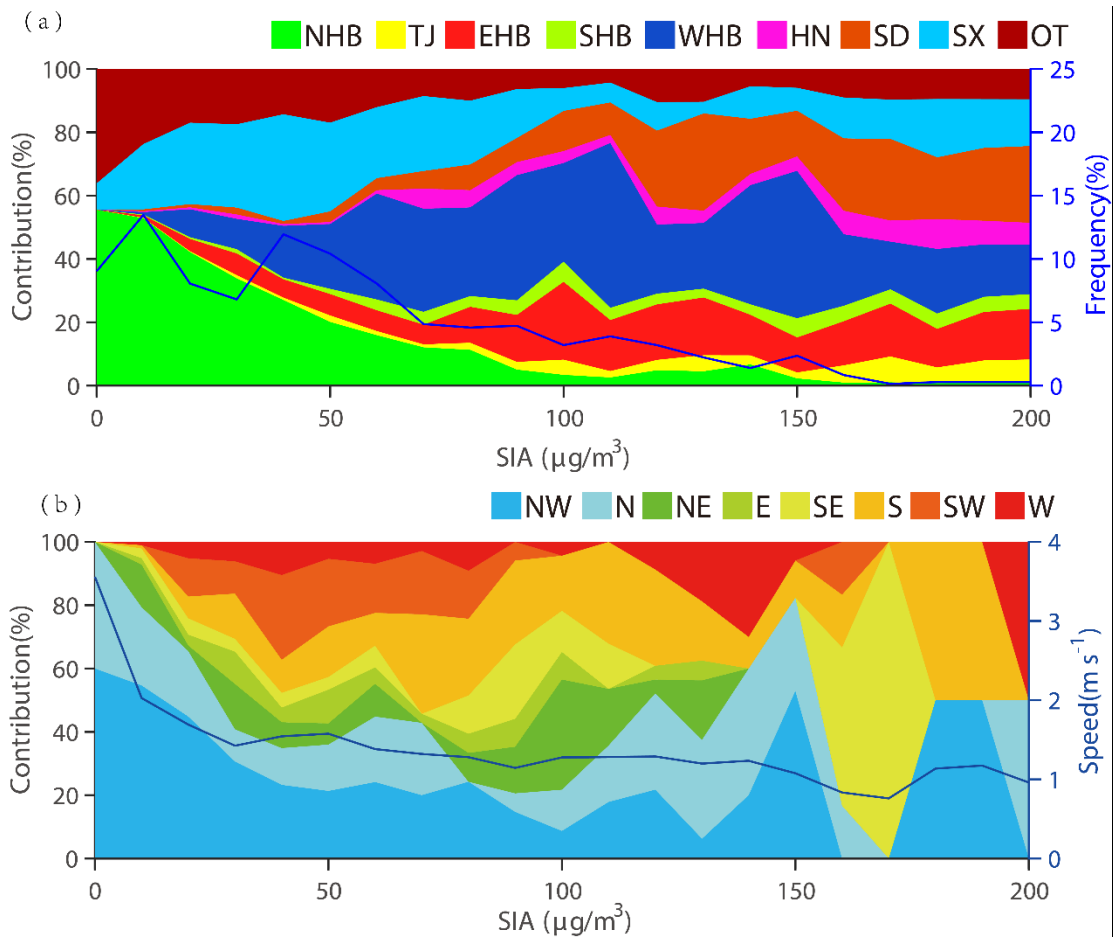


872
 873 **Figure 6.** The contribution of regional transport and local emissions to the average (a)
 874 total PM_{2.5}, (b) secondary inorganic aerosols (SIA), (c) primary inorganic aerosols (PIA,
 875 including BC and primary inorganic PM_{2.5}) over BTH area. The numbers above the pie
 876 represent average concentrations (μg m⁻³) of certain species in certain cities.
 877



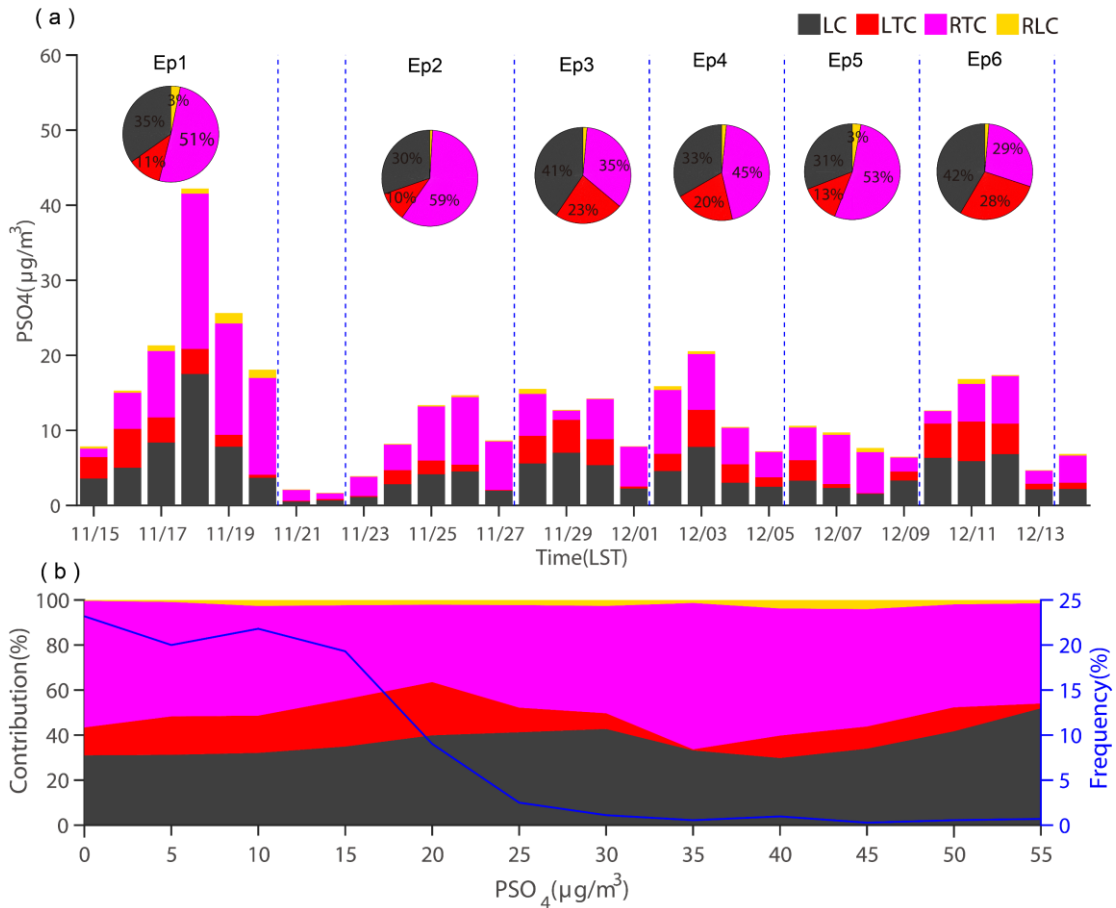
878

879 **Figure 7.** (a) Source contribution of PM_{2.5} in Beijing and pies represent average status
 880 of each episode; (b) Relative contribution of different regions to SIA, OM and PIA in
 881 Beijing at the surface layer during each episode (shaded). Concentrations are also
 882 shown (blue line).



883

884 **Figure 8.** (a) Relative contribution of regionally transported SIA under different
 885 pollution levels in Beijing during the whole study period; (b) Variation of wind
 886 directions under different pollution levels in Beijing during the whole study period.



887

888 **Figure 9.** (a) Sources of secondary sulfate in Beijing. (b) Variation of secondary sulfate

889 sources with surface sulfate concentration in Beijing for the whole study period. LC

890 means sulfate locally produced from Beijing emitted SO₂; LTC refers to sulfate

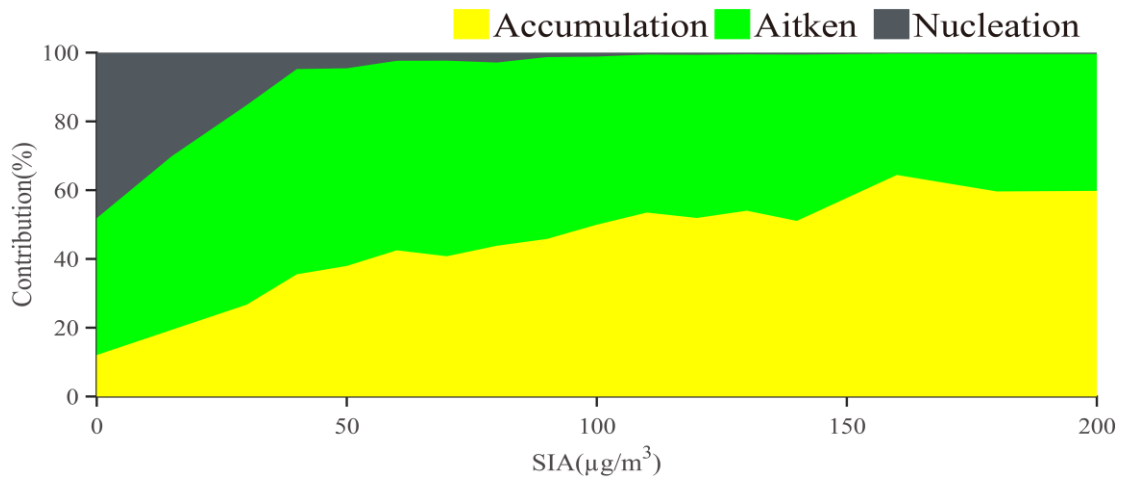
891 chemically formed in regions except Beijing from the Beijing emitted SO₂; RTC is

892 sulfate chemically formed in the transport pathway to Beijing from SO₂ emitted in

893 source regions except Beijing; RLC is sulfate produced in regions except Beijing from

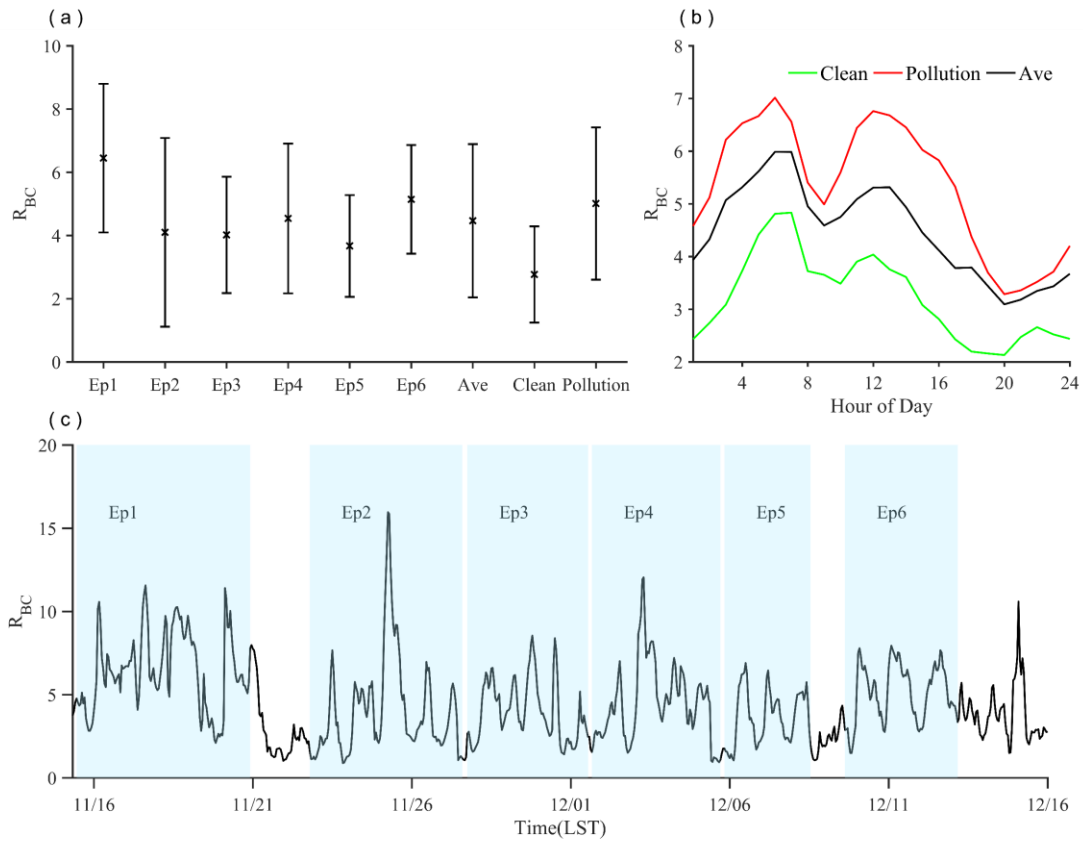
894 locally emitted SO₂ and transported to Beijing.

895



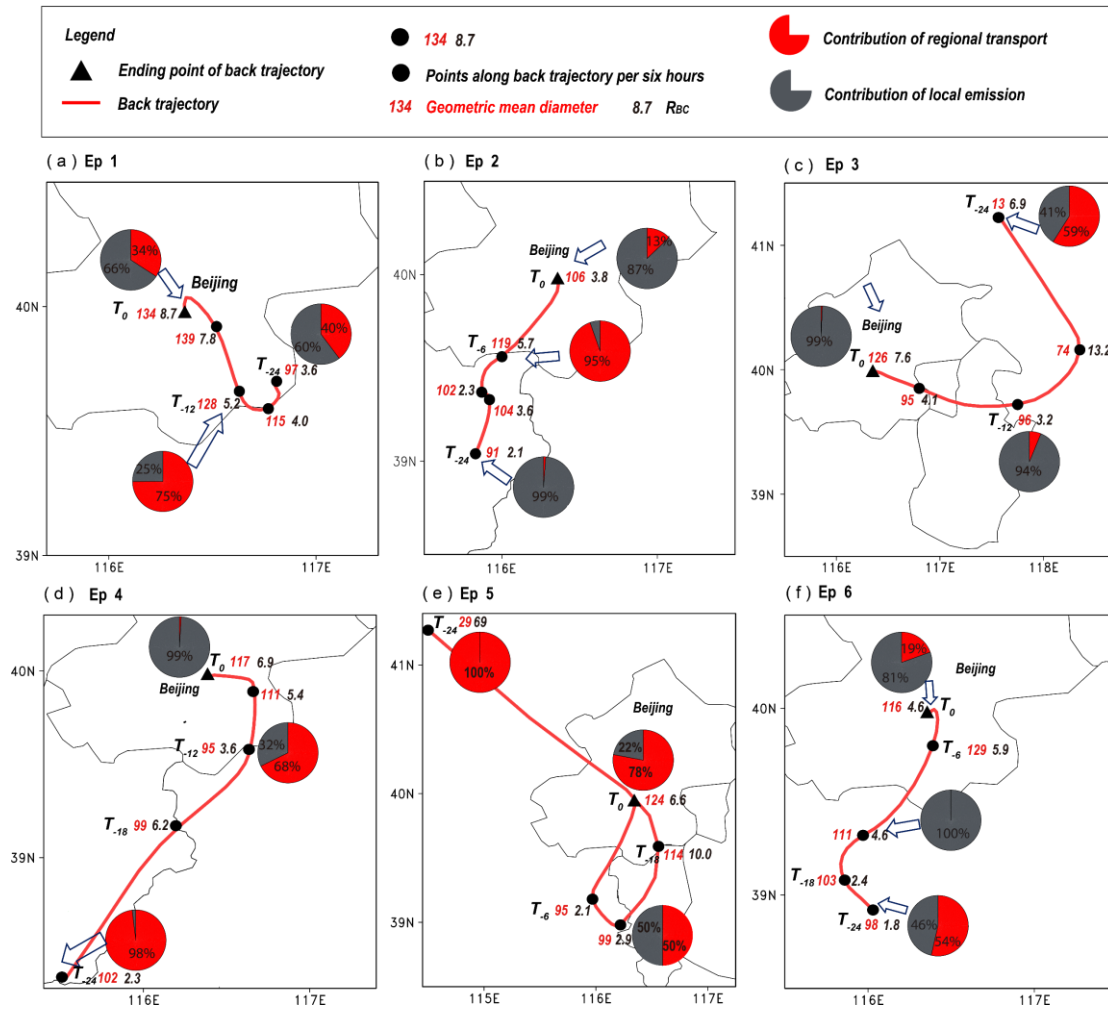
896

897 **Figure 10.** Variation of number concentration fraction of particles with SIA in Beijing
 898 during whole study period.



899

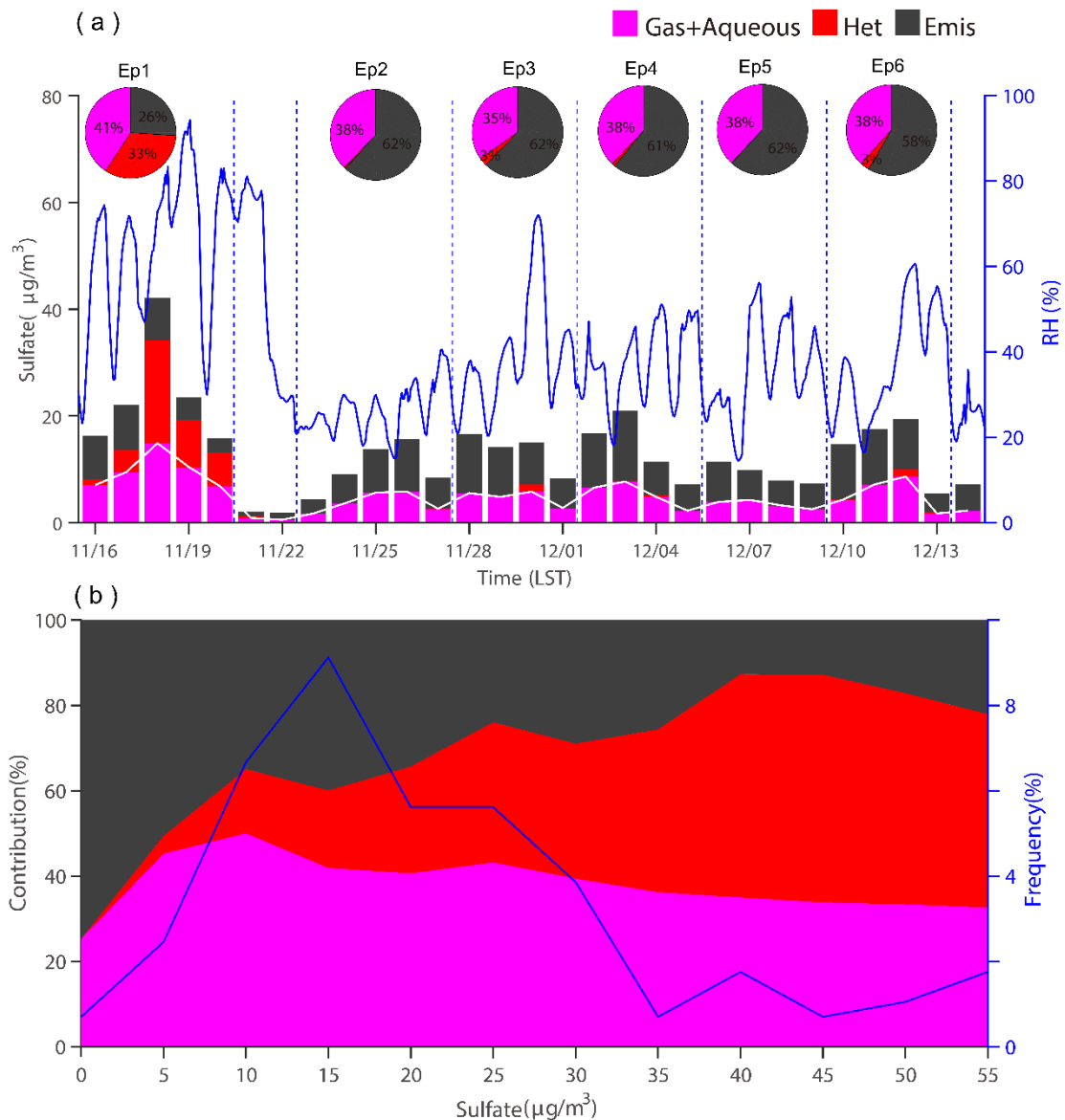
900 **Figure 11.** (a) average and standard variation of massing ratio of coating to BC (R_{BC})
 901 during different episodes and pollution levels, (b) diurnal cycles of R_{BC} under different
 902 pollution levels, (c) temporal variation of R_{BC} during study period.



903

904 **Figure 12.** Variation of aerosol properties along transport. Panel a–f refers to episode
 905 1–6. The red lines refer to 24 h backward trajectories at the altitude of 100 m. Aerosol
 906 properties include geometric mean diameter (GMD [nm], red numbers beside the solid
 907 blocks), mass ratio of coating to BC (R_{BC} , the black numbers beside the solid blocks,
 908 an indicator of aging degree), region source of BC (pies, the red represents regional
 909 transport and the gray is the local contribution). Solid black triangles are ending points
 910 of back trajectories, called T_0 . Solid black circles are points along trajectories per six
 911 hours. T_{-6} , T_{-12} , T_{-18} , T_{-24} mean 6, 12, 18, 24 hours before arriving at ending site. Ending
 912 times of back trajectories are before pollution peaks at 21:00 on November 18, 22:00
 913 on November 25, 16:00 on November 29, 22:00 on December 03, 0:00 on December 8
 914 and 22:00 on December 11 (LST), respectively.

915



916
 917
 918
 919
 920
 921
 922
 923
 924
 925
 926
 927
 928

Figure 13. Contribution of different formation ways to sulfate in Beijing. (a) Daily average. Blue line shows relative humidity at Beijing. Pies show average contribution of different ways during each episode. (b) Relationship between sulphate concentration and different formation pathways of sulphate during Ep1.

929 **Tables**

930 **Table 1.** Source-tagging regions and primary PM_{2.5} emissions during 15 November–15
931 December, 2016 in this study. ^a

Regions	Descriptions	Area 10 ³ km ²	Population 10 ⁶	GDP ^b (10 ¹² CNY)	Emission ^c (10 ⁹ g)
BJ	Beijing	16.4	21.7	2.5	3.6
TJ	Tianjin	11.9	15.6	1.8	3.9
NHB	Chengde, Zhangjiakou and Qinhuangdao	84.1	11.6	0.4	3.6
WHB	Baoding and Shijiazhuang	38.0	21.2	0.9	8.1
BTH	EHB Tangshan, Langfang and Cangzhou	33.9	20.3	1.1	10.1
	SHB Hengshui, Xingtai and Handan	33.3	22.9	0.7	6.8
HN	Henan	167.0	95.3	4.0	26.6
SD	Shandong	155.8	99.5	6.8	38.5
SX	Shanxi	156.7	36.8	1.3	25.9
OT	Other regions				

932 ^a Regions are shown in Fig. 1c.

933 ^b GDP unit in 2016 is Chinese Yuan (CNY) (<http://www.tjcn.org/tjgb/>).

934 ^c PM_{2.5} emissions data are obtained from the 2016 Multi-resolution Emission Inventory for China
935 (MEIC) with 0.25° × 0.25° resolution.